TECHNISCHE UNIVERSITÄT WIEN
Vienna University of Technology

Formic acid photoelectroreforming on bismuth vanadate based catalysts

Master Thesis

CONDUCTED AT THE

GROUP OF MOLECULAR AND MATERIALS CHEMISTRY

INSTITUTE OF MATERIALS CHEMISTRY

VIENNA UNIVERSITY OF TECHNOLOGY

BY

STEFAN SEMIR PFAFFEL, BSC

UNDER SUPERVISION BY

UNIV.PROF. MAG.RER.NAT. DR.RER.NAT. DOMINIK EDER

AND

UNIV.ASS. DR.RER.NAT. DOĞUKAN H. APAYDIN

For those who have to suffer
unimaginable pain and fear
while I am writing this

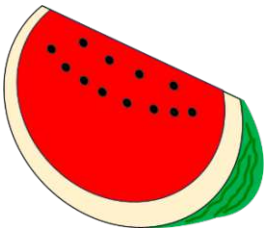

Abstract

Hydrogen storage materials are a key factor in implementation of a sustainable hydrogen economy.[1] Among many options, liquid organic hydrogen storage (LOHC) materials are of high interest due to their easy handling and implementation to existing infrastructure. A possible candidate for LOHC is formic acid (FA), a low toxicity, water miscible compound that can also be found in nature.[2] Furthermore, a key advantage is the possibility of implementing a carbon neutral cycle by coupling carbon dioxide (CO_2) reduction to FA with selective FA oxidation to CO_2.[3]

For the oxidative part of aforementioned cycle, most research up to now has focused on FA photoreforming over titanium dioxide (TiO_2)[4-7], a UV absorbing semiconductor, but little effort has been made to implement a semiconductor with absorption in the visible light range, such as bismuth vanadate ($BiVO_4$), which recently has gained attention due to its capabilities for oxygen evolution reaction.[8-10] This thesis focuses on utilisation of $BiVO_4$ as a photocatalyst under applied external potential.

Preliminary experiments were conducted in search of metal co-catalysts for support of the photocatalytic reaction on TiO_2. The same metal co-catalysts were then introduced to $BiVO_4$ based samples for use under photoelectrocatalytic conditions.

It was found, that both copper (Cu) and (Ni) were suitable for selective photoreforming of FA to CO_2 over TiO_2 under UV illumination (365 nm). Furthermore, $BiVO_4$ showed to be a selective catalyst for the oxidation of FA to CO_2 under photocatalytic conditions (solar spectrum) with applied external potential of 0.4 V vs. reversible hydrogen electrode (RHE). It was then examined if Cu and Ni were also applicable as co-catalysts on $BiVO_4$ under photoelectrochemical conditions. While addition of Copper co-catalyst to $BiVO_4$ lead to unstable material, introduction of Ni as a co-catalyst was successful, showing promising results for the reduction of required energy for photoelectrochemical oxidation of FA over $BiVO_4$.

Staturory declaration

I hereby declare that the thesis submitted is my own unaided work, that I have not used other than the sources indicated, and that all direct and indirect sources are acknowledged as references. This printed thesis is identical with the electronic version submitted.

Vienna, ../../….

Table of Contents

1. Introduction

1.1. Towards a sustainable energy economy

When talking about a clean and ecological energy economy that is future-proof in terms of humanity's subsistence on a planet with limited resources, one of the first terms that comes to mind is hydrogen. The concept of a hydrogen-based energy economy became a popular idea over the past few years, and has often been praised as the solution for energy crisis and climate change[11], even as early as 50 years ago[12]. The idea hereby is to produce hydrogen, useable as a fuel, from electrolysis of water, which is powered by means of renewable energy. Hydrogen produced in this manner is called *green hydrogen*.[13] Nowadays, even on the consumer level, products based on hydrogen energy, such as hydrogen cars, utilising a fuel cell for generation of electrical energy, have become available.[14]

However, currently applied hydrogen production techniques further add to the problematics of energy crisis and climate change, as about 95%[15] of currently produced hydrogen is so-called *grey hydrogen*, produced by processes like steam reforming from fossil energy sources, which themselves emit carbon dioxide (CO_2)[16], the greenhouse gas with the highest absolute impact due to the sheer volume produced by humanity's industrial processes.[17]

Grey hydrogen can be relabelled *blue hydrogen*, if carbon capture methods are used subsequentially after the steam reforming process to capture the produced CO_2. This intermediate state of hydrogen production is highly favoured by companies involved in the fossil-based energy sector as it would still require their involvement in the energy sector in general, however, *blue hydrogen* does not represent a sustainable way of energy production as fossil sources are still involved.[13]

This leads to the conclusion that *green hydrogen* is the way to pursue to ensure a sustainable energy system in the future. However, at the current state the renewable energy sources considered most efficient are solar and wind energy, which are both highly dependent on location and surrounding conditions.[18] Therefore, the produced hydrogen by electrolysis needs to be stored, which is a rather difficult task in the case of hydrogen, because of its light weight and low energy density in gaseous state. This is especially critical for mobile applications of hydrogen storage, where both high volumes and high weight are unfavourable properties.[1]

Currently, several techniques for hydrogen storage are explored by researchers, among which are physical methods such as compression in gaseous state, liquification, cryocompressing and physical adsorption, as well as chemical hydrogen storage in metal hydrides, complexes or in

liquid organic molecules. Physical methods are well established from a technical point of view but have drawbacks such as high energy cost for compression in case of compressed gaseous hydrogen, boil-off losses that can only be avoided by expensive insulation in case of liquified hydrogen and a combination of the aforementioned drawbacks in case of cryocompression, which on the other hand delivers higher energy densities. Physical adsorption methods suffer from low adsorption rates at ambient temperatures.[1]

Chemical storage methods have in common, that no extreme pressure and temperature is needed for operation, as it is the case for liquified and compressed hydrogen. Metal hydrides usually offer a hydrogen content of 1-2 mass%, while hydride complexes can offer higher mass contents, such as Lithium borohydride ($LiBH_4$) with a mass content of hydrogen of 18.5%. A main drawback of metal hydrides is the slow hydrogen extraction kinetics. These are in most cases attributed to impurities in the feed hydrogen as well as contamination in the storage material and limitations for the heat exchange involved.[19] The main disadvantages of hydride complexes are the high operating temperature for release of hydrogen as well as the irreversibility of the release reaction.[20]

The main advantage of liquid organic molecules as hydrogen storage materials is their feasible storage at ambient conditions in simple fuel tanks, as it is already implemented for bulk chemical products and in cars, making at least partial recycling of existing infrastructure possible.[21] Several organic substances can be considered for this application, such as formic acid.

1.2. Formic acid as a carrier for hydrogen

Recent developments show that formic acid is a promising candidate as a carrier molecule for hydrogen. Firstly, formic acid contains a relatively high amount of hydrogen of 4.4 mass%. As the simplest carboxylic acid, it possesses low toxicity and is a clear liquid at room temperature[2, 21], making it easy to handle. Currently, two ways of formic acid decomposition are known, as depicted in Scheme 1. The dehydration pathway leads to carbon monoxide (CO) and water (H_2O) as decomposition products, whereas the dehydrogenation pathway produces CO_2 and hydrogen (H_2).[2] For the role of formic acid as a carrier for hydrogen, the dehydrogenation pathway is preferred, which makes a selective catalyst only exhibiting the dehydrogenation an interesting material. This is especially relevant, if the produced hydrogen is intended for use in fuel cells, where even trace amounts of CO are able to deactivate the fuel cell catalyst by poisoning.[3]

$$H_2O + CO \xleftarrow{dehydration} HCOOH \xrightarrow{dehydrogenation} H_2 + CO_2$$

Scheme 1: Formic acid decomposition pathways

A further advantage of formic acid, compared to hydrogen storage materials such as hydride complexes, is the reversibility of the dehydrogenation process by hydrogenation of the produced CO_2[3], whereas both hydrogenation and dehydrogenation can be conducted under mild conditions.[21] Therefore, a carbon neutral cycle can be evolved.

1.3. State of art

Several approaches have been examined in the past utilising the dehydrogenation pathway. Primarily, these can be divided into homogeneous and heterogeneous catalytic approaches. While homogenous approaches show their typical advantages in turnover rate and selectivity, the separation of catalyst from the product remains a challenge[3], especially when scaled up to industrial quantities.[21] Heterogenous approaches classically can be divided into thermocatalytic, photocatalytic and electrocatalytic methods, utilising different driving forces for carrying out the desired reactions, as well as combinations of these.

Out of those, photocatalytic methods or combinations including those are of special interest as it is possible to directly harvest energy from sunlight for implementation of chemical reactions. In all cases, semiconductors play a key role in implementation of photocatalytic techniques.[22]

1.3.1 Semiconductors in formic acid oxidation

Semiconductors, as well as insulators, are materials possessing a Fermi level energy sitting in a so-called band gap, an energy region of the material's electronic structure not occupiable by electrons, that is enclosed by two energy bands, energetic regions which are possible to be occupied by electrons. The band with higher energy is usually referred to as conduction band (CB) while the band sitting at lower energy than the band gap region is referred to as valence band (VB). Because of the Fermi level sitting right between those two bands, VB is occupied with electrons while CB is empty. This, however, is only true at 0 K since electrons are able to be excited from VB to CB by energy quants. The band gap can therefore be described as the energetical difference between VB and CB. There is no sharp distinction between semiconductors and insulators in terms of bandgap width.[23] For this thesis, every material with a bandgap below 5 eV is considered a semiconductor. 5 eV corresponds to a wavelength of 247 nm, meaning that the wavelength spectrum of sunlight reaching the surface of the earth is mostly covered by this energy region.[24]

Excited electrons leave a vacancy in VB, often referred to as a hole (h^+). The electron-hole-pair, also referred to as exciton, is not bound anymore to a specific energy state in VB, but can spatially move, making the material conductive upon excitation. In case of some semiconductors, thermal excitation by ambient conditions is sufficient for significant

conductivity.[25] The exciton can quench if the electron falls back from CB to VB, this usually happens after a certain time upon excitation.[23] However, the recombination process does not have to happen by quenching, as the electron can also be utilised on its path down the energy drain for a chemical redox reaction, whereas the electron is transferred to the reduced compound while the oxidised compound gives off an electron to the semiconductor to 'refill' the hole.[26] Scheme 2 depicts this process.

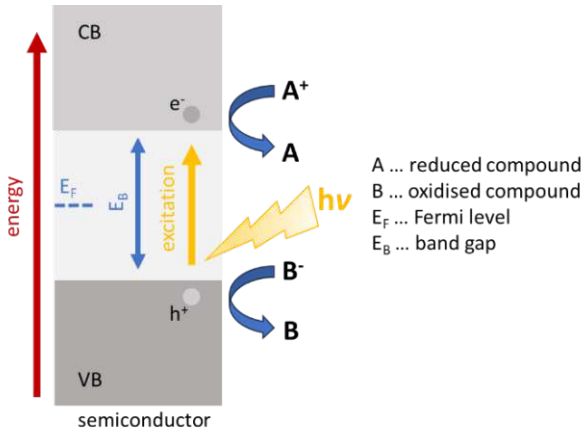

Scheme 2: Principle of a photocatalytic process

A further distinction can be made between p- and n-type semiconductors, whereas the former shows intrinsic defects above 0 K leading to holes in the valence band such as cation vacancies or dopant ions of higher valence while the latter show intrinsic defects above 0 K leading to excess electrons in the conduction band, such as anion vacancies.[23]

1.3.2 Titanium Dioxide

Titanium dioxide (TiO_2) is a widely researched semiconductor material in the field of photocatalysis due to several advantages such as non-toxicity, chemical stability and low cost.[27] Three crystal modifications are known, anatase, rutile and brookite, whereas the former tetragonal anatase is the modification most commonly used in photocatalysis applications due to higher photoactivity and negative conduction band potential. The intrinsic bandgap of 3.2 eV corresponds to a wavelength of 387 nm, meaning that UV-light is needed for excitation of electrons to the conduction band.[28] Due to its tendency towards oxygen vacancies, TiO_2 usually acts as a n-type semiconductor making it more interesting for oxidising applications.[26]

TiO_2 has been examined in the past for formic acid photochemical reforming. It was found that the ratio of (101) to (001) surface in anatase nanoparticles has strong influence on the reaction rate.[4] TiO_2 prepared by a sol-gel method showed to allow lowering of formic acid splitting voltage under photoelectrochemical conditions.[5, 29] Also, flow cell reactors have been implemented for performing of the desired reaction.[6]

The biggest disadvantage of TiO_2 is the absorption wavelength in the UV region, which is impractical regarding applications utilising sunlight directly. A typical approach to at least partially overcome this disadvantage is bandgap engineering.[26] However, alternatives with absorption energies in the visible range are of great interest.

1.3.3 Bismuth Vanadate

In recent years bismuth vanadate ($BiVO_4$) has gained popularity throughout the photocatalysis community due to the beneficial energetic position and size of the bandgap of its monoclinic scheelite modification, with 2.4 eV bandgap, corresponding to a wavelength of 517 nm sitting well in the visible range, and the CB edge sitting at a potential of 2.4 V in relation to the reversible hydrogen electrode RHE, meaning that in theory a sufficient potential for oxygen evolution reaction (OER) is given. In reality, monoclinic bismuth vanadate possesses several disadvantages with hindsight to photocatalytic applications, such as a high recombination rate for excitons as well as poor electrical conductivity. Both properties influence photocurrent, which is the enhancement of the current under applied external potential in case of illumination with photons at energies higher than the bandgap energy. In the past, researchers have been able to increase the photocurrent of $BiVO_4$ by co-doping with other metal species such as Molybdenum or Tungsten.[9, 10] Nonetheless, the advantageous band gap position and comparably simple synthesis strategies[30] render monoclinic $BiVO_4$ an interesting candidate for engineering efficient photocatalysts. Other modifications, such as zircon-type $BiVO_4$ show higher band gap energies. The lower bandgap of scheelite type $BiVO_4$ is attributed as a consequence of the Bi-6s orbitals causing a VB edge closer to the CB edge constructed by V-3d orbitals.[8]

1.3.4 Metal co-catalysts

Opposed to semiconductors, the Fermi-level of metals lies in an energetically non-forbidden zone, making metals electrical conductors even at temperatures close to 0 K. This also makes electrons from metals readily available for reaction partners, allowing for efficient electron transfer in catalytic reaction. Especially noble metals have been used for decades in catalytic applications, as they can easily exchange electrons with their surroundings without being oxidised and decomposing.[31] Metals can therefore be used as an electron mediator between the photoactive semiconductor material and target reactants, as depicted in Scheme 3. The excited electron of an exciton is consumed oxidising compound A^+ to A. The hole in the valence band is filled with an electron from the metal co-catalyst, which can also be described as the hole moving from the valence band of the semiconductor to the Fermi-level of the metal. Here the hole is readily available as an oxidising agent, transforming compound B^- to its oxidised form B.

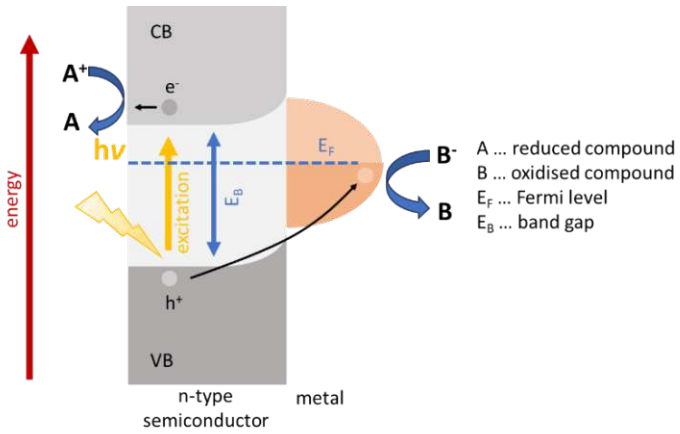

Scheme 3: Electron-hole transfer between photoactive n-type semiconductor and target reactant via metal co-catalyst

Establishing contact between a metal and a semi-conductor leads to a Schottky junction, where the Fermi levels of the two materials adjust to each other, leading to a band-bending effect in the semiconductor area close to the material interface, as depicted in Scheme 3. The direction of band-bending depends on the type of semiconductor (n- or p-type) and the relative positions of the Fermi levels. This band bending can act as a kinetic inhibition to both electrons and holes, depending on the energetic direction of the band-bending, but it can also direct the path of the electron or hole and allow for more efficient charge separaton.[26] In the given example, the excited electron is directed away from the semiconductor-metal interface because of the 'upwards'-band-bending of the n-type semiconductor.

1.3.5 Application of external potential – electrochemistry

In some cases, the energy utilised from recombination of an exciton, the bandgap energy (see 1.3.1) is not sufficient. The reason for this can be both of thermodynamic nature, if the energy difference between educts and products of the desired reaction is bigger than the bandgap energy, or it can be of kinetic nature, if the energy required to overcome a kinetic barrier on the reaction pathway is bigger than the bandgap energy. In those cases, application of external potential can be a tool to overcome the additional energy barrier.

In practical use, external potential is applied as external voltage on the examined material, now acting as a working electrode. For this, a counter electrode must be introduced, as well as some kind of electrolyte connecting the two electrodes to be able to construct a closed circuit. This causes a spatial separation of oxidative and reductive reactions. If oxidative potential is applied to the working electrode, then the reduction will happen at the counter electrode and *vice versa*. The electrons generated by the oxidation travel as electrical current through the external circuit to the reducing electrode. By convention, the oxidising electrode is called *anode* and the reducing electrode is called *cathode*.[23] In Scheme 4, a simple 2-

electrode setup is depicted showing the location of oxidative and reductive reactions on their related electrodes.

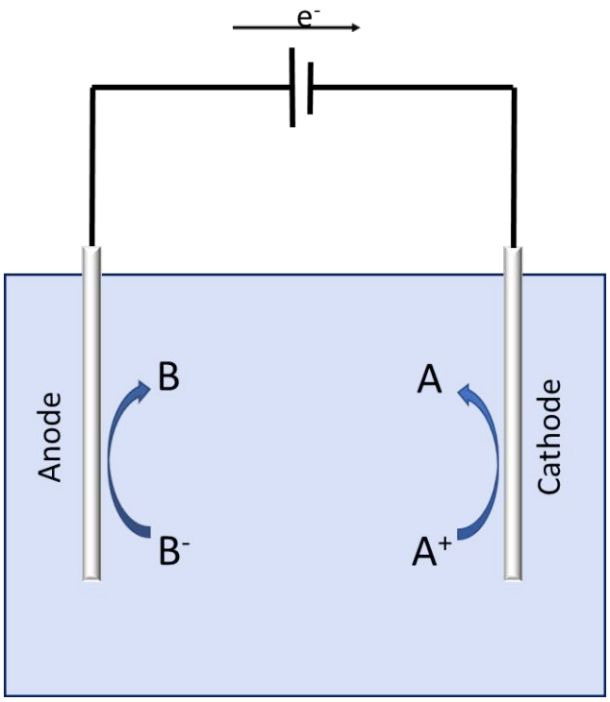

Scheme 4: 2-electrode electrolysis setup. A is the reduced compound, B is the oxidised compound. ©Dorottya Varga

In addition, a third electrode not experiencing any current flow and therefore not taking part in the electrochemical reaction can be introduced. This electrode can be kept at a constant potential difference to one of the other two electrodes (working electrode) by varying the potential between the other two electrodes, acting as a reference point. Therefore, the third electrode is usually referred to as reference electrode, making use of half reactions with well-known potentials with respect to the arbitrarily defined zero point of the reversible hydrogen electrode (RHE). This system consisting of working electrode (WE), reference electrode (RE) and counter electrode (CE) is referred to as 3-electrode-system for dynamic electrochemical measurements. Introduction of a reference electrode makes not only precise setting and monitoring of electrolysis potentials possible, but also allows for electrochemical material characterisation by recording the measured current dependent on the set reference potential.[32]

1.4. Motivation

Introduction of a carbon neutral cycle utilising formic acid as liquid organic hydrogen carrier is of high interest. Most research on this topic is focused on the selective CO_2 reduction reaction to formic acid, while the oxidative part of this cycle is comparatively neglected. Research so far has been focused on thermocatalytic formic acid reforming as well as on

photoreforming on Titanium dioxide (TiO_2) based catalysts. No research has been conducted on introducing visible light photocatalysts to the knowledge of the author.

The task of this thesis was to examine Bismuth vanadate ($BiVO_4$), a prominent visible light photocatalyst, for its possible application in formic acid reforming, opening the path for efficient sunlight utilisation for the desired reaction. Catalyst selectivity towards the dehydrogenation pathway is of high importance for this application. Furthermore, possible efficiency increase by application of co-catalysts was to be examined. For this, Copper (Cu) and Nickel (Ni) were to be examined for their applicability in formic acid photoreforming on TiO_2 and then transferred to $BiVO_4$.

Finally, material characterisation was to be conducted using X-ray diffraction (XRD), X-ray photoelectron spectroscopy (XPS) and scanning electron microscopy with energy dispersive X-ray analysis (SEM/EDX).

2. Experimental Methods

2.1. List of chemicals

Chemical formula	Name	CAS number	Purity
NH_4OH	Ammonia	7664-41-7	25%
H_2O_2	Hydrogen peroxide	7722-84-1	30%
--	Hellmanex®	--	--
$(CH_3)_2CO$	Acetone	67-64-1	technical grade
$(CH_3)_2CHOH$	iso-Propanol	67-63-0	technical grade
C_2H_5OH	Ethanol	64-17-5	technical grade
--	Ethyl cellulose	9004-57-3	--
TiO_2	Aeroxide® P25	13463-67-7	99.5%
$C_{10}H_{17}OH$	Terpeniol	8000-41-7	anhydrous
$CuSO_4 \times 5\ H_2O$	Copper sulfate pentahydrate	7758-99-8	--
$Cu(ac)_2 \times H_2O$	Copper acetate hydrate	6046-93-1	--
$Ni(ac)_2 \times 4\ H_2O$	Nickel acetate tetrahydrate	6018-89-9	98%
KI	Potassium Iodide	7681-11-0	--
$C_6H_4O_2$	1,4-Benzoquinone	106-51-4	99%
C_2H_5OH	Ethanol	64-17-5	absolute
HNO_3	Nitric acid	7697-37-2	65%
$Bi(NO_3)_3 \times 5\ H_2O$	Bismuth nitrate pentahydrate	10035-06-0	98%
$VO(acac)_2$	Vanadyl acetylacetonate	3153-26-2	99%
C_2H_6SO	Dimethyl sulfoxide	67-68-5	technical grade
$Ni(acac)_2$	Nickel acetylacetonate	3264-82-2	95%
$C_{18}H_{35}NH_2$	Oleylamine	112-90-3	70%
$C_{24}H_{51}N$	Tri-n-octylamine	1116-76-3	97%
HCOOH	Formic acid	64-18-6	98%
NaOH	Sodium hydroxide	1310-73-2	80%
Na_2SO_4	Sodium sulfate	7757-82-6	--
H_2SO_4	Sulfuric acid	7664-93-9	96%

2.2. List of devices

Drying and calcination processes were carried out using a Nabertherm LT5/12 muffle oven capable of temperatures between 30 and 3000 °C.

Annealing processes under inert gas were carried out in a glass tube oven regulated by a Eurotherm 2416 controller.

Light sources used for photodeposition methods as well as for photoelectro- and photochemical methods were ThorLab Solis 365C for UV light and 3C for visible light experiments.

Electrochemical experiments, including depositions, voltammetric methods and chronoamperometric methods were carried out on a PalmSens4 potentiostat utilising PSTrace5 software. For cyclic voltammetry and chronoamperometry measurements, a Perfectlight double chamber H-cell with NAFION® separation membrane was used. All electrochemical measurements involving a 3-electrode setup made use of a Perfectlight Ag/AgCl 3.3 M KCl reference eletrode.

Scanning electron microscopy (SEM) images were acquired using FEI Quanta 250 FEG scanning electron microscope to obtain information on the morphology of the samples. Energy dispersive X-ray analysis (EDX) could be carried out simultaneously.

X-ray diffraction measurements (XRD) were carried out on a XPERT II:PANalytical XPert Pro MPD to obtain data on the crystal structure of the synthesized samples directly on their substrates at different stages of the synthesis and of reference substances and educts to acquire a valid comparison and assure their purity. Measurements were carried out using a Cu X-ray source (8.04 keV, 1.5406 Å) with Bragg-Brentano geometry while the sample holder was rotated around the z-axis. Measured spectra were then compared to reference spectra obtained via the software HighScore.

X-ray photoelectron spectroscopy (XPS) was carried out on a custom-built SPECS XPS-spectrometer equipped with a monochromatised Al-Kα X-ray source (µFocus 350) and a hemispherical WAL-150 analyzer (acceptance angle: 60°).

pH measurements were conducted on a Mettler Toledo SevenMulti pH and conductivity measurement device equipped with an AMEL 411/CGG/12 combined pH Ag/AgCl reference electrode with 3.3 M KCl.

Gas chromatography was carried out using a Shimadzu Nexus GC-2030 gas chromatograph equipped with a BID detector.

2.3. Synthesis

All samples were synthesised on glass slides covered with a layer of fluorine-doped tin oxide (FTO; layer thickness 300 µm) on one side. Prior to sample application, the glass slides underwent a cleaning process in an ultrasonic bath consisting of the following steps:

- 45 min in NH_4OH 25% solution in water, with addition of H_2O_2 30% solution in H_2O (10 ml) 15 min before the end of this step
- 30 min in Acetone (technical grade)
- 30 min in Hellmanex 2% solution in water
- 30 min in DI water
- 30 min in iso-propanol

For TiO_2, several application methods for the metal co-catalysts Cu and Ni were explored, starting with a published photodeposition method.[7] The aim hereby was to create a reliable synthesis method leading to well-performing catalysts, that could then be applied on $BiVO_4$ based samples.

2.3.1 Titanium dioxide

Titanium dioxide-based specimen were obtained by utilising a published spin-coating method.[33] Ethyl cellulose (5.010 g) was dissolved in EtOH (50 ml) by alternation between sonification and stirring under slight heating for 4 h and consecutive stirring for 72 h. Part of the obtained solution (2.03 g) was added to TiO_2 (P25, 409.9 mg) as well as Terpeniol (isomer mix, 1.75 ml) and EtOH (4 ml) and the obtained suspension was stirred for 12 h.

Substrate material were FTO covered glass slides with a size of 1 × 3 cm^2, with 1 cm^2 covered by Kapton tape. The remaining 2 cm^2 were fully covered with the TiO_2 suspension. Spincoating was then conducted at 3000 min^{-1} for 1 min. Spin-coated samples were dried (100 °C for 20 min) and calcinated (400 °C for 120 min).

2.3.1.1 Drop-cast Cu/TiO_2

$Cu(ac)_2 \times H_2O$ (20.1 mg, 0.10 mmol) was dissolved in EtOH (100 ml). 150 µl of this solution were drop-cast onto a TiO_2-covered FTO. The complete area of the FTO slide (3 cm^2) was covered, leading to a theoretical areal concentration of copper atoms of 0.05 µmol·cm^{-2}. Samples were then dried at 100 °C for 20 min and subsequently calcinated at 150 °C for 120 min.

2.3.1.2 Photodeposited Cu/TiO_2

Photodeposition method was carried out according to and as a modification of a known method.[7]

For replication of the already published method, $CuSO_4 \times 5\ H_2O$ (84.5 mg, 0.338 mmol) and FA (20.0 µl, 24.4 mg, 0.530 mmol) were added to deionized water (50 ml). The obtained solution was used for photodeposition under UV light with a maximum intensity of 3.82 $mW \cdot cm^{-2}$ at 365 nm for 60 min. The sample did not show any visible change upon photodeposition.

For modification, $Cu(ac)_2$ (20.1 mg, 0.10 mmol) was dissolved in EtOH (100 ml). The obtained solution was used for photodeposition under UV light with a maximum intensity of 38.2 $mW \cdot cm^{-2}$ at 365 nm, with EtOH not only acting as a solvent, but also as a sacrificial agent getting oxidised in the process. Deposition times were 5, 20- and 45-min. Samples that had undergone a longer deposition time of 20 and 45 min showed a clearly visible dark gray layer with red edges.

2.3.1.3 Drop-cast Ni/TiO_2

Drop-casting solutions containing Ni precursor were produced for two concentration levels, 1 mM and 20 mM, dissolving $Ni(ac)_2 \times 4\ H_2O$ (24.5 mg, 0.10 mmol) in 100 ml EtOH and (49.5 mg, 0.20 mmol) in 10 ml EtOH, respectively. Theoretical areal concentrations for Ni atoms were calculated to be 0.05 $\mu mol \cdot cm^{-2}$ and 1 $\mu mol \cdot cm^{-2}$, respectively, for dropcasting 150 µl onto 3 cm^2. For both concentrations, samples were subsequently dried (100 °C for 20 min) and calcinated (150 °C for 120 min).

2.3.2 Bismuth vanadate

Bismuth vanadate synthesis was carried out as a modification to a known method, utilising a two-electrode setup instead of a three-electrode setup.[34]

Deionised water (50 ml) was added to KI (3.38 g, 20.4 mmol). The resulting solution was adjusted to pH 1.75 with 6 drops of HNO_3 conc., upon which $Bi(NO_3)_3 \times 5\ H_2O$ (974.3 mg, 2.009 mmol) was added. EtOH abs. (20 ml) was added to p-Benzoquinone (490.3 mg, 4.536 mmol). Upon complete dissolution, they were combined and used for electrodeposition of intermediate material BiOI onto FTO covered glass slides with a size of 3 × 1 cm^2 at a voltage of -1.5 V for 5 min.

For the final synthesis step, DMSO (10 ml) was added to $VO(acac)_2$ (531.4 mg, 2.004 mmol). Upon dissolving, this solution was used as a Vanadium precursor for dropcasting onto the FTO slides covered with BiOI (100 $\mu l \cdot cm^{-2}$). Samples were subsequently dried at 120 °C for 20 min and calcinated at 450 °C for 120 min. Calcinated samples were washed with 0.5 M NaOH to remove excess V_2O_5.

2.3.2.1 Photodeposited $Cu/BiVO_4$

$Cu(ac)_2 \times H_2O$ (26.0 mg, 0.130 mmol) was dissolved in EtOH (100 ml). The solution was used for photodeposition using Solis 3C visible spectrum lamp at 29.8 $mW \cdot cm^{-2}$. The deposition setup is depicted in Figure 1. As for the photodeposition of Cu on TiO_2, EtOH acted both as solvent and sacrificial agent (see 2.3.1.2).

Figure 1: Setup for photodeposition of Cu onto $BiVO_4$

2.3.2.2 Drop-cast $Ni/BiVO_4$

Dropcasting solution containing $Ni(ac)_2$ as precursor at a concentration of 20 mM was produced by dissolving $Ni(ac)_2 \times 4\ H_2O$ (49.5 mg, 0.20 mmol) in 10 ml EtOH. Theoretical areal concentration for Ni atoms was calculated to be 1 $\mu mol \cdot cm^{-2}$ for dropcasting 150 µl onto a FTO glass slide covered with $BiVO_4$ with an area of 3 cm^2. Samples were then subsequently dried (120 °C for 20 min) and calcinated (450 °C for 120 min).

2.4. Characterisation techniques

2.4.1 X-ray diffraction (XRD)

To gain insight on structural features of the synthesized materials, XRD measurements were conducted on several samples directly after synthesis as well as after activity evaluation by photochemical and photoelectrochemical methods. XRD measurements are based on the interaction of X-ray radiation with crystal structures, more precisely on the reflection and diffraction of X-ray beams on crystal plains. This requires the wavelength of the X-ray beams and the distance between the crystal plains to be in the same magnitude. Bragg's equation (Equation 1) shows, that the entrance angle of X-ray beams of a specific wavelength,

interfering positively after reflection on the crystal, is connected to a specific distance of the crystal plains. Therefore, the lattice constants of a crystal in form of a spectrum can be derived from a measurement that emits a constant wavelength of X-ray radiation onto a specimen at a constantly altering angle. The obtained spectrum is characteristic for each crystalline material.[35]

Equation 1: Bragg's equation

$$2 \cdot d \cdot \sin\theta = n \cdot \lambda$$

d … distance between two crystal plains in Å
θ … angle between X-ray beam and crystal plain in °
n … diffraction order
λ … wavelength of the X-ray source in Å

2.4.2 Scanning electron microscopy (SEM)

SEM is an electron microscopy technique using electrons accelerated with energies between 2 – 40 keV that interact with the examined specimen, resulting in back-scattered electrons, secondary electrons, Meitner electrons and X-rays, which can be used for analysis. In the case of this thesis, secondary electrons give the important information about surface topography since they usually provide the best resolution compared to the other products of electron-specimen-interaction.[36]

Analysis of the produced, element-characteristic X-rays was as well utilised for elemental analysis with energy dispersive X-ray spectroscopy (EDX). When electrons accelerated by high voltages, as used in electron spectroscopy, interact with the examined samples, they can either collide with atom nuclei leading to unspecific X-ray bremsstrahlung or they can interact with an electron bound to a specimen atom. In the latter case, the specimen electron gets kicked out of its orbital, leaving a vacancy behind. This vacancy can then be filled by an electron from an energetically higher shell. Transitioning from the higher energetic state to the energetically lower vacancy leads to emission of energy quants. These energy quants are in the wavelength area of X-rays, are element specific, and can therefore be used for chemical analysis. As X-ray photons are emitted in all spatial directions, either analysis of one spot with the diameter of the incident electron beam can be performed, or areal scanning is used to obtain information on the location of certain elements. Combination with SEM consequently makes sense to be able to map the occurrence of certain elements onto topographic information of the sample.[23]

2.4.3 X-ray photoelectron spectroscopy (XPS)

XPS is a standard method in modern material characterisation. The method is based on excitation of electrons in atoms of a sample, that are at or very close to the surface of the material by X-ray radiation. The energy of the X-rays leads to emission of excited electrons that possess a characteristic energy, dependent on energy levels of the atom orbitals in the examined materials. Since neighbouring atoms with different electronegativities influence the binding energy of an electron to a certain atom, oxidation states can as well be analysed. Additional to the emitted photoelectrons with energies varying with the energy of the source, Meitner electrons characteristic to the examined material are as well emitted. These do not vary in energy with the energy of the primary electron source. Qualitative information can then be obtained by measuring the kinetic energy of the emitted electrons based on Equation 2.[37]

Equation 2: Calculation of kinetic energy in XPS measurements

$$E_{kin} = h \cdot \nu - E_B - \Phi$$

E_{kin} … kinetic energy of the emitted photoelectron in eV
h … Planck's constant in eV·s
v … frequency of X-rays used for excitation in s^{-1}
E_B … binding energy of the emitted electron in eV
Φ … work function in eV

2.4.4 Photocatalytic characterisation

Photocatalytic experiments were conducted using a simple setup as shown in Scheme 5 Gas tight vials equipped with septa for gas sample acquisition were filled with electrolyte with a given formic acid concentration. Catalyst material with an area of approximately 0.5 cm^2 was placed in the solution as depicted inScheme 5, so illumination from the bottom by use of a LED lamp was possible. The light irradiation was provided by a ThorLabs Solis-365C with a light intensity of 185.7 $mW \cdot cm^{-2}$ at 365 nm.

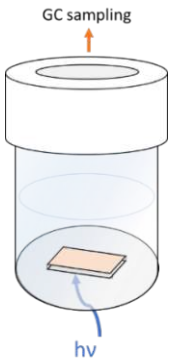

Scheme 5: Sample placement and irradiation direction in photochemical experiments

Gas samples were drawn before, throughout and at the end of every experiment and analysed by means of gas chromatography. Before drawing the first gas sample, reaction cells were purged for 45 min with nitrogen to ensure removal of gaseous as well as dissolved oxygen.

2.4.5 Electrochemical methods

Electrochemical experiments were conducted in H-cell electrochemical glass reactors using a 2-cell 3-electrode setup. A typical 3-electrode setup, as depicted in Scheme 6, consists of a working electrode (WE), a reference electrode (RE), a counter electrode (CE) and an electrolyte as well as a potentiostat used for control of electrical influence on the system by applying a cell potential between the working and the counter electrode to be able to hold a certain reference potential between working and reference electrode. The two cells of the reactor were separated by a NAFION® membrane. Reactor design allowed for external illumination of the working electrode, purging of both cells, and locking them gas-tight, as well as gas and liquid sample acquisition through septa from both cells. In all experiments, WE was the examined material, RE was an Ag/AgCl (3M KCl) reference electrode and CE was a 1 × 1 cm^2 platinum sheet.

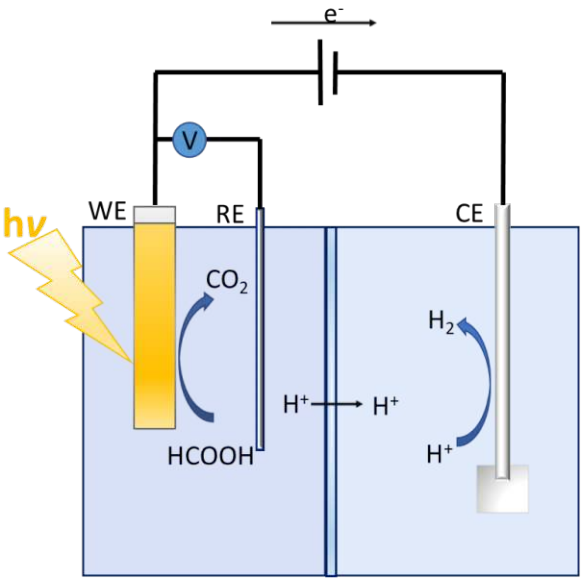

Scheme 6: 3-electrode electrochemical setup used for (photo)electrocatalytic experiments. ©Dorottya Varga

2.4.5.1 Cyclic voltammetry (CV)

CV is an important method in electrochemistry and is used to determine oxidation and reduction mechanisms of examined electrochemical systems. The electrochemical system, in case of this thesis consisting of a working electrode, a counter electrode and an electrolyte, is hereby exposed to a linear sweep of voltage at a constant rate, between two fixed vertex potentials, forth and back for a number of cycles. Current is recorded and plotted over potential, giving diagrams with current dependent on the voltage. Peaks in such a diagram

indicate potential-dependent processes in the system, usually oxidation or reduction processes. Other potential-dependent processes include adsorption and desorption processes as well as phase transitions.

In case of a CV measurement examining one single, reversible electrochemical reaction, the shape of the plotted current over potential is usually referred to as “duck-shape”. To understand this shape, and further CVs with more complex graphs in general, the Nernst-equation (Equation 3) must be considered.

Equation 3: The Nernst-equation

$$E = E^0 + \frac{R \cdot T}{n \cdot F} \cdot ln \frac{(Ox)}{(Red)}$$

E … potential of the electrochemical cell in V
E^0 … standard potential in V
R … ideal gas constant in $J \cdot mol^{-1} \cdot K^{-1}$
T … Temperature in K
n … number of electrons taking part in the reaction
F … Faradaic constant in $C \cdot mol^{-1}$
(Ox) … concentration of the oxidised species
(Red) … concentration of the reduced species

This equation can be read in two directions. On one hand, if the concentration of the oxidised species is the same as the concentration of the reduced species, E equals E^0. On the other hand, this means that if $E = E^0$ is applied to the system, the oxidised and reduced species will stay in an equilibrium state at the same concentration value. Exceeding E over E^0 to higher potentials will favour the concentration of the oxidised species, meaning oxidation takes place. Lowering E below E^0 favours reduction.

In practical applications, E^0 is formally replaced with the experimentally available $E_{1/2}$, which is the mean value of the peak position between the oxidative and reductive sweep of a plotted CV.[38]

In case of this thesis, CVs were used to determine the potential of desired electrochemical processes such as the oxidation of formic acid to CO_2, as well as for material characterisation by observing material characteristic redox processes. Furthermore, CVs were conducted with and without light irradiation to be able to characterise the difference caused by irradiation on a photoelectrode.

2.4.5.2 Linear sweep voltammetry (LSV)

LSVs are based on the same principle as CVs with the only difference being that LSVs consist of a single sweep only from the most oxidative to the most reductive potential or *vice versa*. As with CVs, in case of this thesis, LSVs were conducted with and without light irradiation. As CVs in principle contain the same data as LSVs, LSVs were not further analysed. However, they were always part of the series of electrochemical measurements of one sample to keep measurements comparable.

2.4.5.3 Photoelectrocatalytic characterisation

For photoelectrocatalytic methods the same 3-electrode H-cell setup was used as shown in Scheme 6 for chronoamperometry (CA). A constant potential was applied for a certain amount of time under light irradiation to perform the desired oxidation of formic acid to CO_2. In all cases, light irradiation was provided by a Thorlabs Solis-3C light source at a light intensity of 133.4 $mW \cdot cm^{-2}$. In Figure 2 the used setup is depicted. The applied potential was set, according to the results from CV and LSV measurements, higher than determined $E_{1/2}$ of the desired reaction.

Important measures taken from those experiments are the current throughout the experiment, which, in ideal case, is a measure of the reaction rate, as well as the cell potential. The cell potential can be used to rule out certain reactions that can occur as competing reactions to the desired one, for example water splitting (Equation 4), which can theoretically happen if the cell potential exceeds 1.23 V.[25]

Equation 4: Water-splitting reaction

$$2\,H_2O \rightarrow 2H_2 + O_2$$

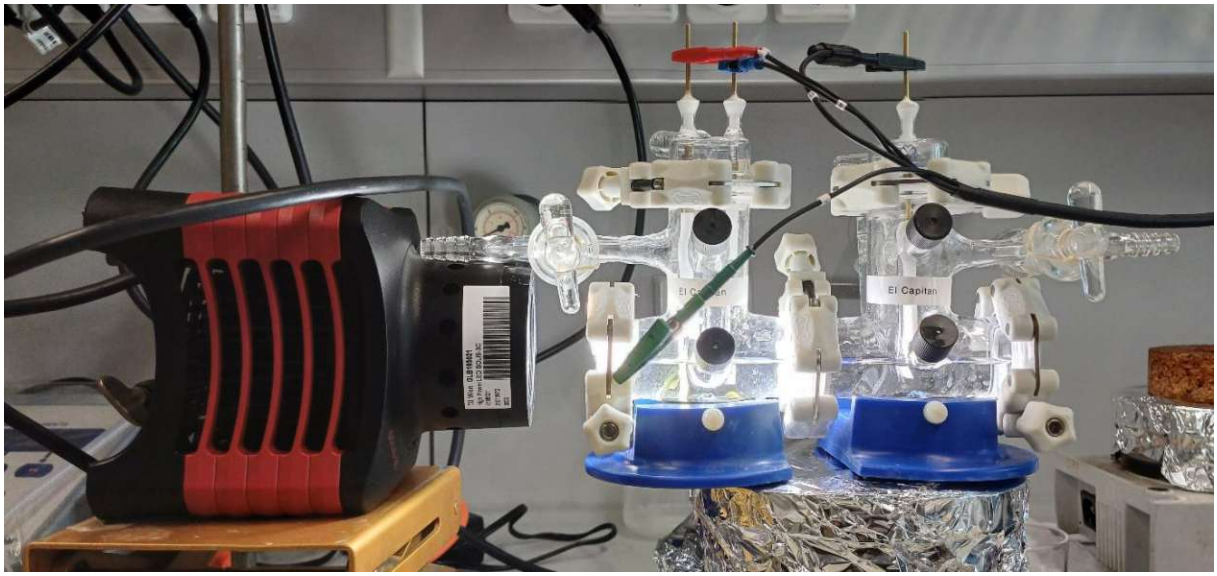

Figure 2: Setup for photoelectrochemical measurements

Furthermore, gas samples were taken before and after every chronoamperometry measurement to determine changes in the headspace caused by the reaction. These samples were taken from both cells of the H-cell setup. On the side of the working electrode, CO_2 concentrations were measured and on the side of the counter electrode, H_2 concentrations were measured. This makes sense assuming that on the working side, Equation 5 takes place, leaving behind 2 protons in solution that migrate to the counter side to form H_2 on the Pt counter electrode (Equation 6).

Equation 5: Oxidative formation of CO_2 from FA

$$HCOOH \rightarrow CO_2 + 2e^- + 2H^+$$

Equation 6: Reductive formation of H_2 from protons

$$2H^+ + 2e^- \rightarrow H_2$$

3. Results and Discussion

3.1. Synthesis and material characterisation

3.1.1 Synthesis

Photodeposition of a Cu precursor on TiO_2 from sulfate precursor in aqueous solution has been published before. Despite longer deposition times and higher educt concentration, no colour shift on the TiO_2 surface was observed (Figure 3), as it was stated in the original publication.[7]

Figure 3: Photodeposited Cu/TiO_2 sample from aqueous precursor

To avoid the need for an energy intensive calcination step, used in the method for drop-cast Cu co-catalyst, an ethanol solution of acetate precursor was used for photodeposition. This worked at higher rates than the deposition from aqueous solution of sulfate precursor, as the ethanol not only acted as a solvent, but also as a highly abundant sacrificial agent. Deposition rates for this method were high enough to lead to visible copper precipitate on the substrate, as it can be seen in Figure 4.

Figure 4: Photodeposited Cu/TiO_2 samples from acetate precursor in ethanol solution. Deposition times from left to right: 45, 20, 5 min

Application of Ni as an alternative co-catalyst to copper was successful with application of a dropcasting method, whereas the two different concentration levels lead to visibly different outcomes on the substrate, as the sample with a higher concentration of Ni co-catalyst of 1 µmol·cm^{-2} showed a grey colour shift, opposed to the sample with a lower concentration of 0.05 µmol·cm^{-2}, as it can be seen in Figure 5.

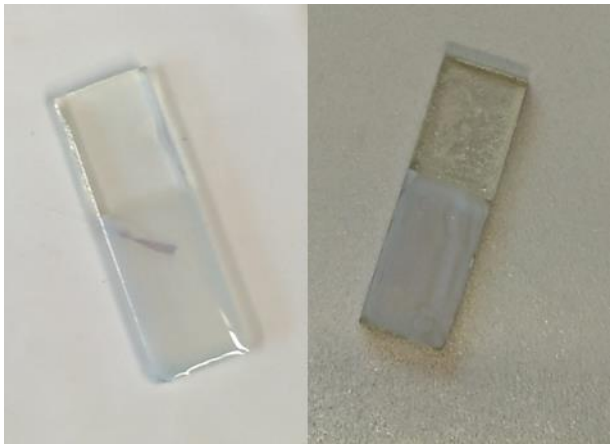

Figure 5: Drop-cast Ni/TiO_2 samples; 0.05 µmol·cm^{-2} on the left; 1 µmol·cm^{-2} on the right

Photodeposition of Cu onto $BiVO_4$ from ethanol solution of acetate precursor was similarly effective as on TiO_2. Co-catalyst precipitation was visible with the bare eye, as it can be seen in Figure 6. The reason for the stripe-shaped deposition pattern is unclear, a possible explanation could be a dependence of the deposition of the angle of light incidence, whereas varying light incidence angle could be the consequence of light refraction on the solvent surface or on other interfaces throughout the path of the light.

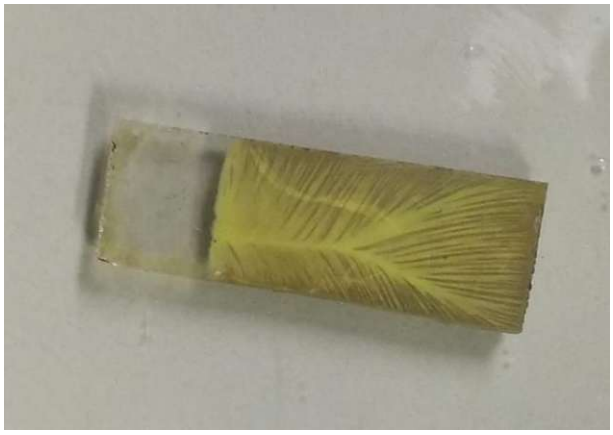

Figure 6: Photodeposited Cu/$BiVO_4$ sample

For application of Ni on $BiVO_4$, the simple dropcasting method for the application of Ni from acetate precursor onto TiO_2 was adopted for $BiVO_4$.

The dropcasting method led to a grey colour shift, as it was observed for the same application method of Ni on TiO_2. Similarly, this method showed to be simple and reproducible, therefore drop-cast Ni/$BiVO_4$ was the focus of this thesis.

3.1.2 Material characterisation

3.1.2.1 TiO_2-based material

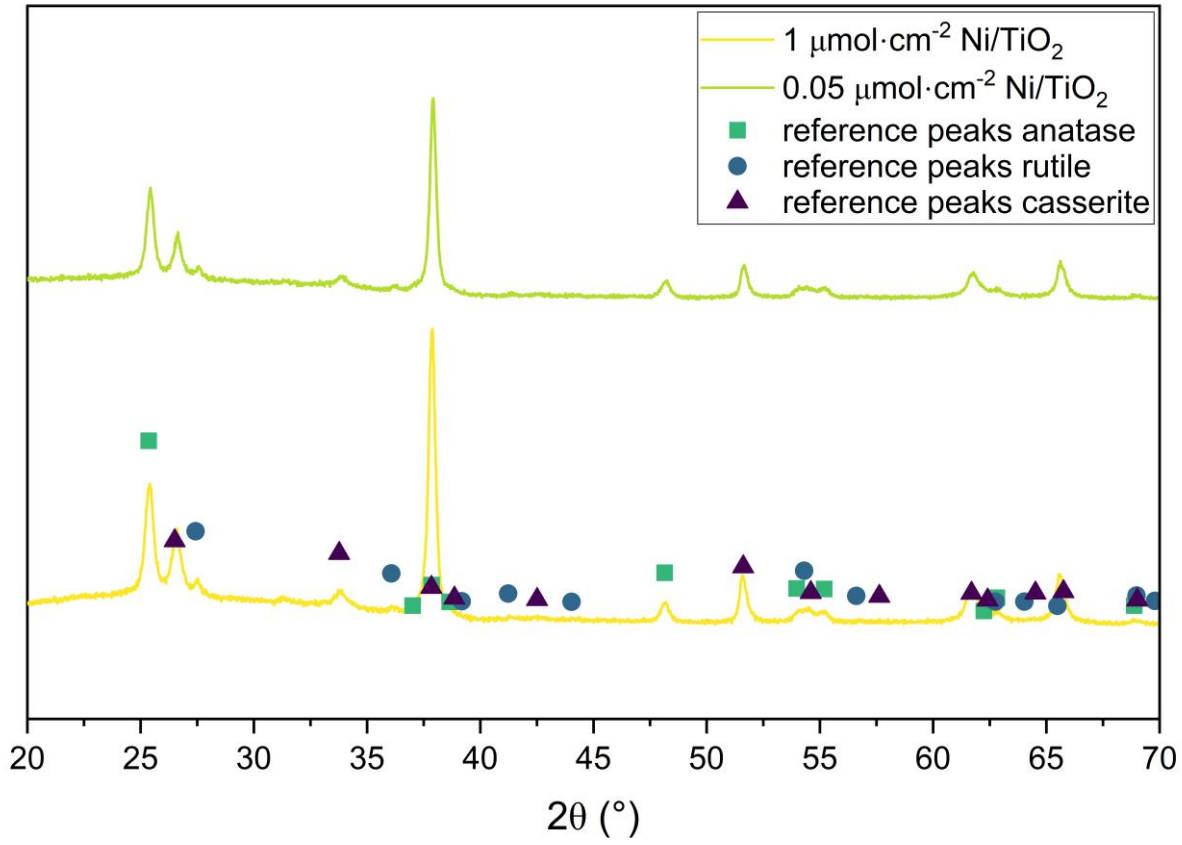

Figure 7: XRD spectra of drop-cast Ni/TiO_2 samples with different co-catalyst loadings 0.05 µmol·cm^{-2} and 1 µmol·cm^{-2}. Reference peaks for anatase, rutile and casserite (SnO_2 substrate) are superimposed to the bottom spectrum.

Titania-based samples Ni co-catalyst with concentration values of 0.05 µmol·cm^{-2} and 1 µmol·cm^{-2} were analysed using XRD. Obtained diffractograms are presented in Figure 7. By comparison with reference data, the presence of TiO_2 in its modifications anatase and rutile was confirmed, as well as the SnO_2 modification casserite.[39] This was expected as the base material for the synthesis of the titania-based samples was Aeroxide® P25 and the sample substrate was fluorine doped tin oxide.[40]

For both precursor concentration steps, drop-cast Ni/TiO_2 samples showed no sign of Ni application in the XRD spectra after synthesis.

3.1.2.2 $BiVO_4$-based material

Material characterisation of $BiVO_4$-based material was conducted using XRD, SEM/EDX and XPS. XRD analysis confirmed the presence of monoclinic bismuth vanadate in both bare $BiVO_4$ and drop-cast Ni/$BiVO_4$ by comparison with reference data[41], as it can be seen in Figure 8 (A). In Figure 8 (B), a comparison between XRD spectra of bare $BiVO_4$ and drop-cast Ni/$BiVO_4$ is

presented, unveiling the presence of NiO as a separate phase on the samples by diffraction peaks at 37 and 43° 2θ NiO(111) and NiO(200), respectively.[42]

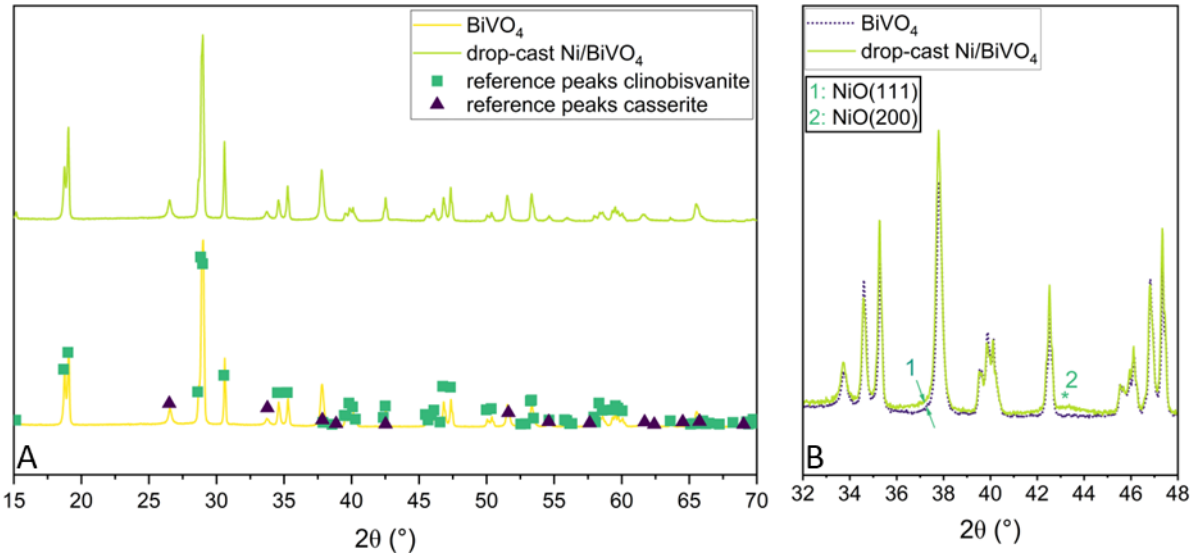

Figure 8: (A) XRD spectra of bare $BiVO_4$ (bottom) and drop-cast Ni/$BiVO_4$ (top). Reference peaks for clinobisvanite and casserite are superimposed on the bottom spectrum. (B) Detailed comparison of bare $BiVO_4$ and drop-cast Ni/$BiVO_4$

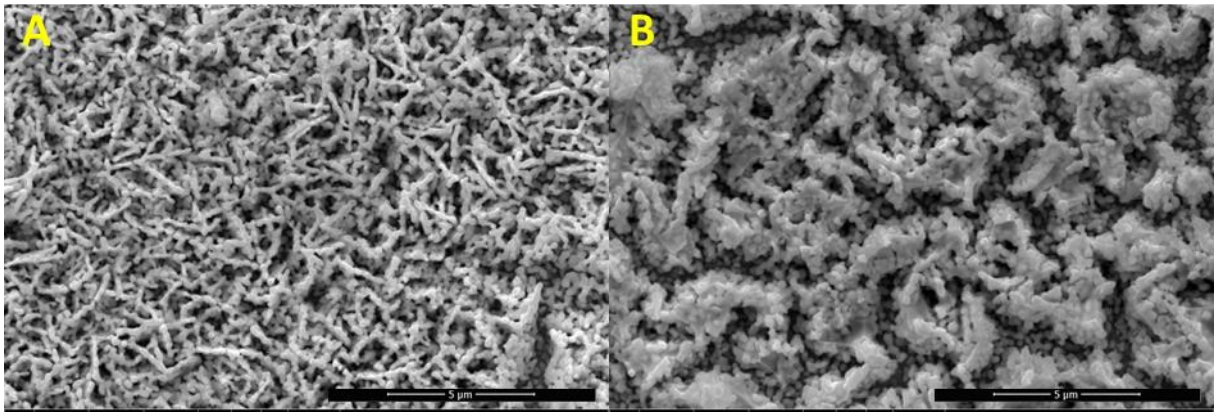

Figure 9: SEM images at 20000× magnification of (A) bare $BiVO_4$ as synthesised (B) drop-cast Ni/$BiVO_4$ as synthesised

In Figure 9 SEM images of bare $BiVO_4$ and drop-cast Ni/$BiVO_4$ are presented. Bare $BiVO_4$ possessed a porous, worm like structure which is a consequence of the electrodeposition method applied for synthesis.[34] Application of Ni to $BiVO_4$ showed by formation of bowl-like precipitates on top of the base material.

Energy dispersive X-ray spot analysis was conducted on all samples examined by SEM, confirming the successful synthesis of $BiVO_4$ according to the measured atom ratios, as well as presence of Ni in aforementioned bowl-like precipitates. Spot analysis of the bowl-like structures unveils high Ni content in proximity of those structures, indicating appearance of the co-catalyst as a separate phase. In these precipitates, usually atomic ratios of 2:1 O:Ni and higher were detected. Therefore, it cannot be confirmed that the applied co-catalyst appears in the form of NiO from this analysis, but it is rather safe to say that Ni appears in some oxide

form. Spot analysis not conducted in direct proximity to the bowl-like structures confirms the expected atomic ratios Bi:V:O 1:1:4. Detailed reports of these analyses can be found in the appendix (7.4). Additionally, to examine the distribution of elements on the distinct precipitates of drop-cast Ni/$BiVO_4$ samples, EDX mapping was performed. In Figure 10 the EDX maps resulting from this analysis are superimposed onto an SEM image of drop-cast Ni/$BiVO_4$. On the left side, a map of all detected elements is presented (green = Sn; red = Bi; pink = V; orange = Ni). On the right side, only the regions of high Ni signal intensity are mapped. The shown images are not raw data, but colour intensities have been raised to allow for increased contrast and visibility.

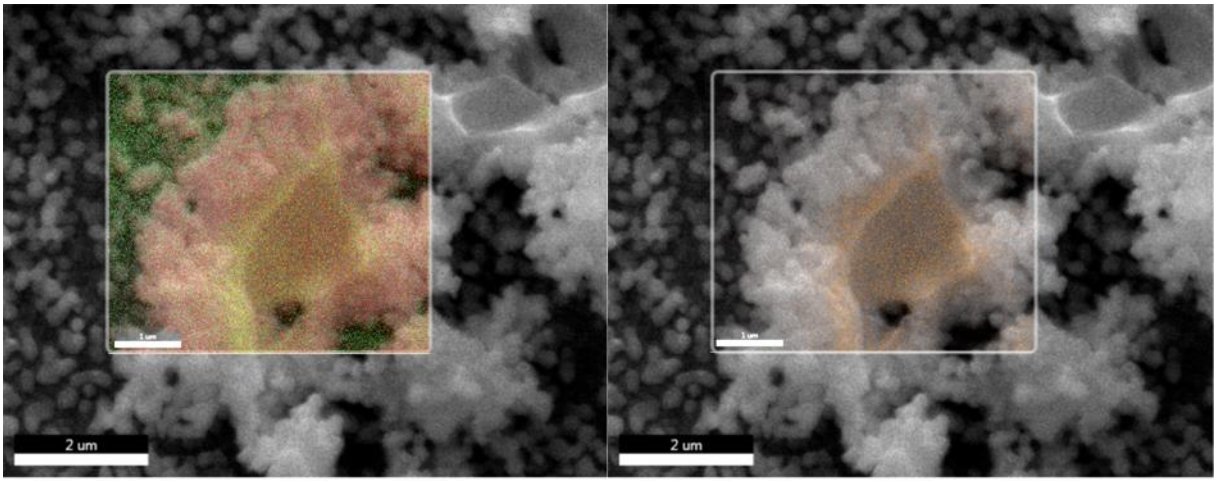

Figure 10: EDX map overlay with SEM pictures of pristine drop-cast Ni/$BiVO_4$ at a magnification of 40000; Left: All elements detected; Right: spots of high Ni signal intensity only (orange).

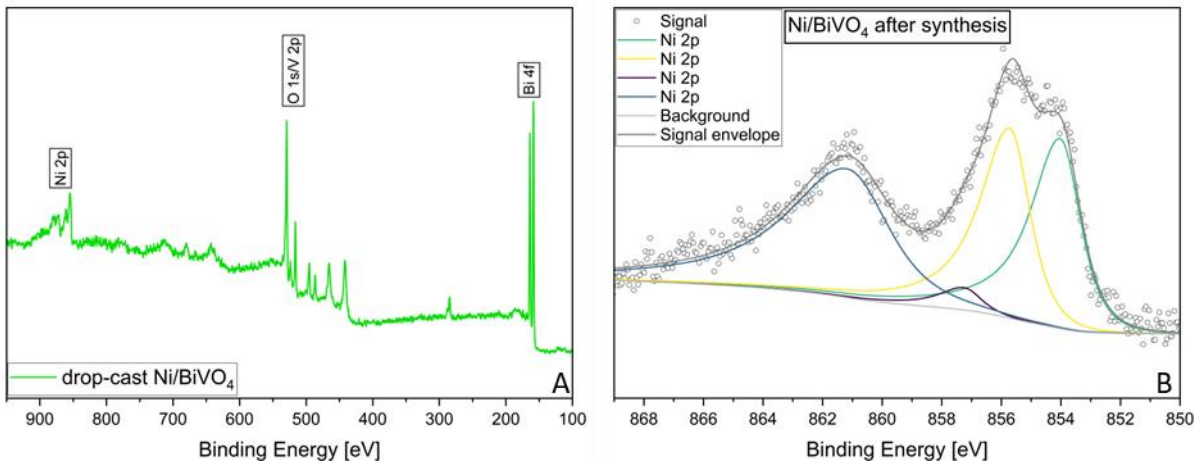

Figure 11: XPS spectra of drop-cast Ni-BiVO4 sample (A) survey spectrum (B) detail of the area of Ni 2p signal

In order to identify the nature of the oxides XPS analysis was performed. XPS data of drop-cast Ni/$BiVO_4$ material is presented in Figure 11. Figure 11 (A) shows a survey scan over an energy range of 100 to 950 eV, with peaks corresponding to Bi, V, O and Ni labelled accordingly. Figure 11 (B) shows a detail of the energy region specific to the Ni 2p signal.

Comparison with reference data[43] once more confirmed the presence of Ni as NiO in oxidation state +2.

Table 1: Quantitative XPS data for drop-cast Ni/$BiVO_4$ material

Orbital	Position in eV	rel. At. %
O 1s / V 2p	529.3	77.06
Bi 4f	158.8	12.77
Ni 2p	854.8	10.17

In Table 1, data from quantitative analysis by XPS measurement of drop-cast Ni/$BiVO_4$ is presented. Due to the close energetic position of O 1s and V 2p orbitals, these are given as one value. The ratio of Bi:(V+O):Ni was measured to be roughly 1:8:1. Assuming the predominance of Ni in the form of NiO, this would mean the ratio of Bi:(V+O) was in the range of 1:7, which is close enough to the theoretical stochiometry of 1:5 (1:1:4) given the uncertainty of O detection due to the overlap with V 2p peaks and possible residues of adsorbed O on the sample surface. The exact identification of the nature of the oxides in NiO_X remains elusive, however due to strong indicators provided by XRD phase analysis and XPS fitting it is assumed that Ni most likely appears as NiO.

3.2. Photochemical characterisation

Photochemical measurements were preliminarily carried out on TiO_2 based samples for exploration of the usability of the chosen metal co-catalysts and their performance based on the utilised synthesis method. The reaction medium was FA solution in water, and the pH of the electrolyte was varied around the pK_a of FA (3.75) to examine whether the protonated or the deprotonated form of FA is advantageous for the desired reaction. Table 2 lists the used samples and experimental parameters for each sample.

Comparison of overall reaction rates ignores change of the reaction rates throughout the reaction and delayed onset of product generation, for example CO. For the TiO_2 based samples, Figure 12 shows a plot of the overall reaction rates for each experiment. In all cases, CO_2 and H_2 were produced right from the start of the experiment, whereas the onset of CO production was delayed differently, depending on the sample type. For the well performing samples Ti-06 and Ti-09, monitored reaction rates calculated from absolute gas concentrations measured by GC sampling are plotted in Figure 13.

Table 2: Experimental list for photochemical experiments

Sample name	Sample type	Reaction medium	Experiment runtime
Ti-01	photodeposited Cu/TiO_2 from aqueous solution and sulfate precursor; 60 min deposition time	10 mM FA adjusted to pH 3.5	103 min
Ti-02	drop-cast Cu/TiO_2	10 mM FA (pH = 2.8)	22 h
Ti-03	drop-cast Cu/TiO_2	10 mM FA adjusted to pH 4.55	22 h
Ti-04	drop-cast Cu/TiO_2	10 mM FA (pH = 2.8)	23 h
Ti-05	photodeposited Cu/TiO_2 from ethanol solution and acetate precursor; 20 min deposition time	10 mM FA (pH = 2.8)	23 h
Ti-06	photodeposited Cu/TiO_2 from ethanol solution and acetate precursor; 45 min deposition time	10 mM FA (pH = 2.8)	19 h
Ti-07	photodeposited Cu/TiO_2 from ethanol solution and acetate precursor; 5 min deposition time	10 mM FA (pH = 2.8)	19 h
Ti-08	drop-cast Ni/TiO_2 with an area concentration of 0.05 $\mu mol \cdot cm^{-2}$	10 mM FA (pH = 2.8)	2.8 h
Ti-09	drop-cast Ni/TiO_2 with an area concentration of 1 $\mu mol \cdot cm^{-2}$	10 mM FA (pH = 2.8)	3.9 h

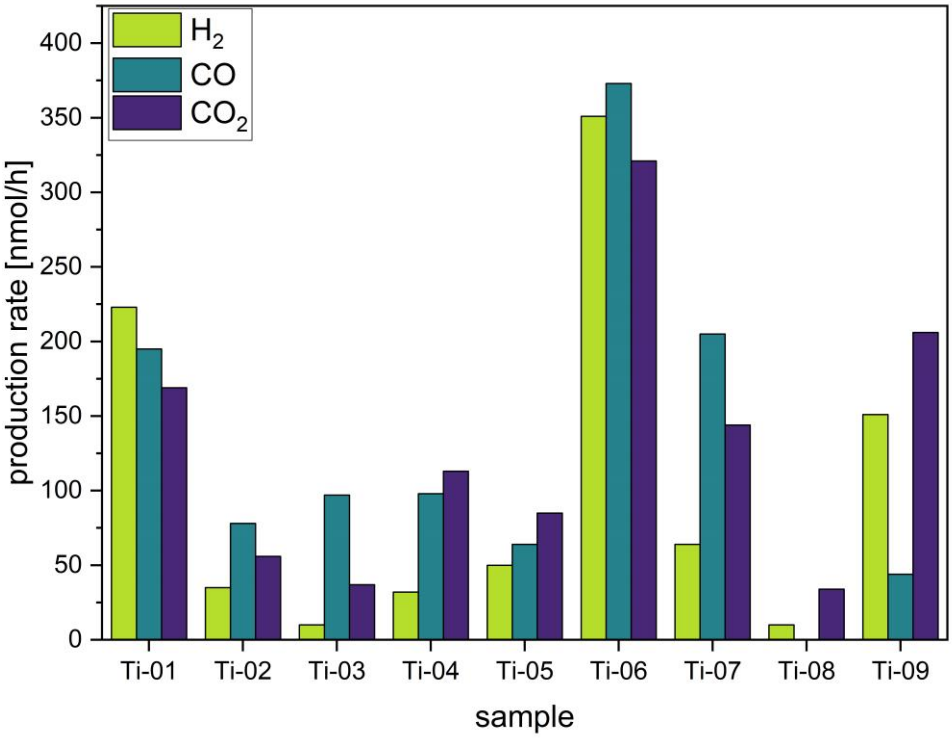

Figure 12: Comparison of overall product generation rates for TiO_2 based samples

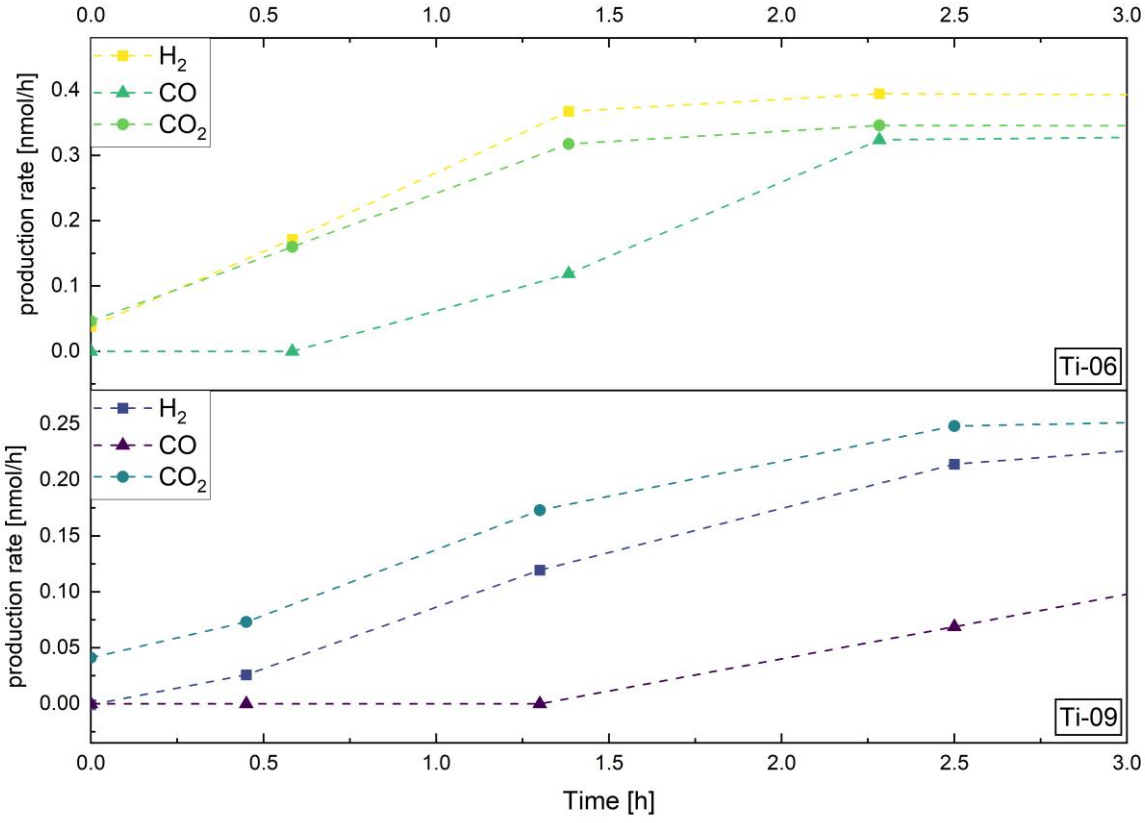

Figure 13: Comparison of product generation rates between a Cu/TiO_2 sample (Ti-06) and a Ni/TiO_2 sample (Ti-09)

Comparison of the overall reaction rates (Figure 12) shows that Ti-06, photodeposited Cu/TiO_2 from ethanol solution of an acetate precursor with a deposition time of 45 min clearly outperformed all other TiO_2 based samples, including materials synthesised with the same method but at lower deposition times. This is not only true for the desired products H_2 and CO_2, but also for CO produced by the inadvertent dehydration pathway of formic acid.

Regarding H_2 production rate, Ti-06 is followed by Ti-01, the sample synthesised according to a published method and at higher pH value close to the pK_a value of formic acid. Similar to Ti-06, Ti-01 performed the product generation of H_2, CO_2 and CO at similar rates. In general, all samples utilising Cu as a co-catalyst show higher rates of CO production in relation to the rates of H_2 and CO_2 production.

Second highest CO_2 production rate was achieved by utilisation of sample Ti-09, drop-cast Ni/TiO_2 with a concentration of 1 $\mu mol \cdot cm^{-2}$, which also performed similar with regards to the H_2 production rate compared to Ti-01. Notably, CO production rate is comparably low for Ti-09.

Considering that the photochemical experiment with Ti-01, leading to the second highest H_2 generation rate, was executed for 103 min, it can be considered that CO production onset was rather early or CO production rate was very high towards the end of the experiment, indicating that catalyst selectivity towards the desired dehydrogenation pathway of formic acid under the experimental conditions applied was rather low for the material synthesised according to a published method.[7] Another explanation may be the reduction of produced CO_2 to CO with Cu acting as the co-catalyst. This would also explain the delayed onset of CO formation.

Ti-02 and Ti-03 not only give information on the performance of drop-cast Cu/TiO_2 catalyst, but also provide an idea of the influence of the protonation state of FA, as pH was adjusted for Ti-03 to 4.55, which lies over the pK_a of FA (3.75) and therefore lead to deprotonated Formate in the educt solution. Over the significantly longer experimental runtime of 22 h, more CO and less H_2 and CO_2 were produced in experiment Ti-03, indicating that under photochemical conditions dehydrogenation pathway may be preferred for the protonated educt. However, overall production rates for both experiments towards the desired H_2 and CO_2 were significantly lower than with Ti-01. Additionally, for both Ti-02 and Ti-03, CO production rate was higher in relation to the products of the dehydrogenation pathway.

As the synthesis of drop-cast Cu/TiO_2 involved an energy demanding calcination step and product generation for this material was lower than with the photodeposited Cu/TiO_2 from sulfate precursor in aqueous solution, modification of the photodeposition method was implemented in search of better performing alternative material. Ti-04 and Ti-05 were carried out in parallel as a comparison between drop-cast material and photodeposited material utilising a modified procedure involving acetate precursor dissolved in EtOH with a deposition

time of 20 min. As noted from comparison between Ti-02 and Ti-03, protonated FA led to higher performance, therefore pH was not adjusted in both experiments. Overall reaction rates indicate rather similar performance. While H_2 and CO generation rates are more favourable with utilisation of the photodeposited material, CO_2 production is higher on the drop-cast material.

Different deposition times for the photodeposition from acetate precursor in ethanol solution were tested for their photoactivity. Ti-06 and Ti-07 were synthesised by the same method, but with deposition times of 45 and 5 min, respectively. pH again was kept unaltered for both experiments. Utilising the sample with low deposition time led to a slightly higher production rate of H_2 overall, but significantly increased production rates for CO_2 and especially CO. As mentioned above, Ti-06 performed the highest overall production rates for all three products.

As the total conversion rate is neglectable for all experiments, it is assumed that the CO reduction onset is not dependent on the educt concentration, but on catalyst degradation.

To examine a second metal as co-catalyst and introduce an alternative to copper, Ni was applied onto TiO_2 by adaptation of the dropcasting method from ethanol solution from acetate precursor. Ni was chosen as it is less active in CO_2 reduction due to the higher binding energy of the metal to CO leading to poisoning of the surface preventing further CO_2 reduction.[44] The dropcasting method was first applied with a resulting concentration on the catalyst of 0.05 $\mu mol \cdot cm^{-2}$ (Ti-08). This material showed comparably low production rates for H_2 and CO_2. However, it was noted that CO production onset had not occurred before 3 h experimental time.

Therefore, dropcasting from a precursor solution with higher concentration was performed, resulting in a concentration of 1 $\mu mol \cdot cm^{-2}$ (Ti-09). Utilising this sample for the photoreforming reaction, H_2 and CO_2 production rates of a similar magnitude as with Ti-01 were achieved while overall CO production rate was low due to the late onset of CO production after 3 h into the experiment.

A comparison of further interest is between Ti-04, drop-cast Cu/TiO_2 and Ti-08, drop-cast Ni/TiO_2, both from an acetate precursor solution of the same concentration. While after 3 h, the gross production of target products CO_2 and H_2 was higher on the Cu based sample, the Ni based sample still showed full selectivity towards the dehydrogenation pathway while CO production onset already had happened on the Cu based sample.

Concluding the above stated, Ti-06 and Ti-09 were the best performing materials with regards to gross production rates. As selectivity is of high interest, Figure 13 shows a comparison between the product generation rates throughout the first three hours experimental time of

samples Ti-06 and Ti-09, clearly showing the later onset of CO production on the Ni/TiO_2 sample, indicating favourable selectivity properties of Ni as a co-catalyst.

3.3. Electro- and photoelectrochemical characterisation

The following materials were examined using electrochemical methods:

- Bare $BiVO_4$ without addition of co-catalyst was examined to find out if the base material is able to catalyse the desired reaction selectively and to set a comparison for the later used samples with attached metal co-catalysts.
- Photodeposited Cu/$BiVO_4$ turned out not to be usable as a catalyst under applied oxidative potential as the photodeposited Cu visibly dissolved due to its relatively low oxidation potential of 0.34 V vs. RHE[25].
- Drop-cast Ni/$BiVO_4$ from acetate precursor turned out to be stable and was the focus of the work as its synthesis is simple and therefore interesting for practical applications. Measurement conditions were systematically changed, and each measurement condition was carried out a total of 3 times to examine the reproducibility of the outcome.

3.3.1 Electrolyte preparation

In all cases, 10 mM FA based electrolyte was used. The electrolyte was always freshly prepared prior to each experiment by adding formic acid (37.4 µl, 46.0 mg, 1 mmol) to water to a total volume of 100 ml. pH was then adjusted to a value between 4.6 and 4.7 (see section 3.3.1.1) by dropwise addition of 0.5 M NaOH. This effectively changes Equation 5 to Equation 7, as the pK_a value of formic acid is 3.75[45], meaning the deprotonated form is predominant at the above stated pH of 4.6 to 4.7. This electrolyte is called **FA electrolyte** throughout this thesis.

Equation 7: Oxidative formation of CO2 from formate

$$HCOO^- \rightarrow CO_2 + 2e^- + H^+$$

To control for the source of the detected products, a comparison electrolyte based on sodium sulfate, with the same ionic strength and pH as the formic acid electrolyte was produced. For exact concentrations, the required amount of NaOH for adjusting the pH of FA electrolyte was determined by three titrations utilising a pH meter. Furthermore, the general equation for calculation of ionic strength (Equation 8) was considered. Sodium sulfate was chosen as both the sodium cation, and the sulfate anion are highly unlikely to react further.

Equation 8: The general formula for calculation of ionic strength[46]

$$I_s = \frac{1}{2} \cdot \sum_{i=1}^{n} c_i \cdot {z_i}^2$$

I_s … ionic strength in M

c_i … concentration of ion i in M

z_i … charge number of ion i

Table 3: Titration values for adjusting pH of formic acid electrolyte

measurement no.	Volume 0.5 M NaOH in ml	pH measured
1	1.75	4.67
2	1.70	4.68
3	1.70	4.69
avg.	1.72	4.68

Values measured for pH adjusting for 3 titrations are listed in Table 3. Based on these, the total volume of a batch of produced formic acid electrolyte was calculated to be 101.72 ml on average. Furthermore, the amount of formate is known to be 1 mmol and from the concentration and volume of NaOH solution, the amount of sodium cations can be calculated (0.86 mmol). From these amounts and the pH value, concentrations of formate, sodium cations and protons were calculated to be 9.83 mM, 8.45 mM and 0.021 mM, respectively. Following Equation 8, ionic strength of the formic acid electrolyte was calculated to be 9.15 mM.

Based on this ionic strength and a pH value of 4.68, desired sodium sulfate concentration for the comparison electrolyte was calculated to be 3.04 mM. This calculation is barely affected by the low proton concentration, therefore in practical application, 3.04 mM Na_2SO_4 electrolyte was produced and then carefully adjusted to the desired pH of 4.6 – 4.7 by dropwise addition of 0.05 M H_2SO_4. This electrolyte is called **comparison electrolyte** throughout this thesis.

3.3.1.1 Determination of desired electrolyte pH

As conducted for the photochemical characterisation (3.2), two comparative measurements were performed for decision on the pH value for the formic acid electrolyte. As stated before, unadjusted 10 mM FA in H_2O possesses a pH value of 2.8, which is below the pK_a value of

formic acid (3.75), meaning that without pH adjustment, formic acid is present predominantly in its protonated form at this concentration.

For comparison, a pH of 4.6 – 4.7 was chosen. This decision is based on buffer theory, stating that a pH step of 1 equals a proton concentration step of one magnitude. At the pK_a of a monovalent acid, protonated and deprotonated form are at the same concentration in equilibrium. In case of 10 mM FA, only the acid is present in the aqueous solution, leading to the above stated pH of 2.8. By addition of NaOH, this pH value is exceeded. As long as the amount of base is below the amount of acid, which is the case as it is known from the titration in 3.3.1, the dependency between pH value and the relation of concentration between protonated and deprotonated acid molecules is given by Equation 9.[25]

Equation 9: Calculation of the pH value of a weak acid

$$pH = pK_a - \log \frac{c_{FA}}{c_{formate}}$$

c_{FA} … concentration of protonated formic acid in mol·l^{-1}

$c_{formate}$ … concentration of deprotonated formate in mol·l^{-1}

From this formula, relation of concentration between protonated and deprotonated form was calculated to be 8.91 for pH 2.8 and 0.11 for pH 4.7, with the latter being the inverse value of the former, indicating that at pH 2.8 the same amount of formic acid is protonated as there is deprotonated formic acid at pH 4.7. Uncertainties of adjusted pH in the range between 4.6 – 4.7 are a consequence of the inaccuracy of pH adjustment.

The comparison of photoelectrocatalytic performance was conducted on drop-cast Ni/$BiVO_4$ samples. Reaction runtime was 2 h under chronoamporometric conditions at a voltage of 0.6 V vs. RHE. Measured CO_2 production rates were 725 nmol·h^{-1} and 783 nmol·h^{-1}, for unadjusted pH and pH 4.66, respectively. Interestingly, H_2 production rate over the Pt counter electrode was as well higher for the experiment with adjusted pH (808 nmol·h^{-1} vs. 57 nmol·h^{-1}). Based on these findings, electrolyte with adjusted pH was used and the comparison electrolyte was produced accordingly, as explained in 3.3.1.

3.3.2 Cyclic voltammetry

3.3.2.1 CV without light irradiation

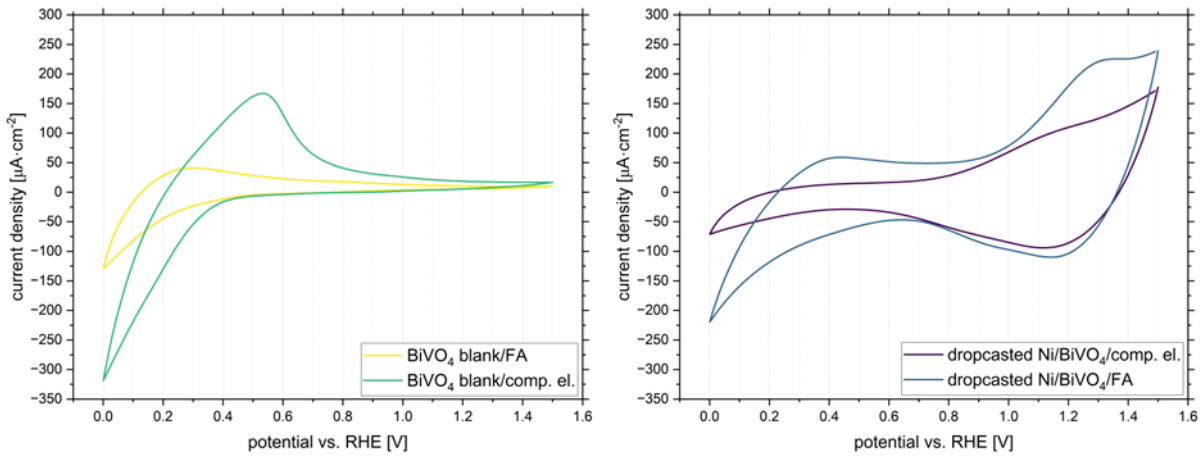

Figure 14: CV comparison of FA electrolyte with comparison electrolyte; left: with bare $BiVO_4$; right: with drop-cast Ni/$BiVO_4$

In Figure 14 (left), a comparison of CVs on bare $BiVO_4$ between FA electrolyte and comparison electrolyte is provided. The most outstanding difference is the irreversible, oxidative peak detected in comparison electrolyte at a potential of over 0.5 V vs. RHE. This peak is attributed to the oxidation of iodide to iodine (Equation 10). This is plausible, as the electrodeposited precursor towards $BiVO_4$ before the final calcination step with $VO(acac)_2$ is BiOI (see 2.3.2), leading to a possibility that there were still traces of iodide left in the sample after one calcination step. This peak cannot be observed in CV plots of samples with Ni co-catalyst as well as in CV plots for bare $BiVO_4$ in FA electrolyte. In case of samples with Ni co-catalyst it is either possible that the second calcination step helps to expel residual iodide from the sample or that the applied Ni performs a redox reaction to oxidise iodide to iodine, that may be supported by the high temperatures of the second calcination step. For the latter case of bare $BiVO_4$ sample in FA electrolyte, it is however rather unclear where this behaviour stems from. Reduction of formate by oxidation of iodide seems unlikely as iodine is thermodynamically rather stable in its reduced form iodide due to its halogenic nature.

Equation 10: Oxidation of iodide to iodine

$$2I^- \rightarrow I_2 + 2e^- \ (+0.54\ V\ vs.RHE)$$

Furthermore, in FA electrolyte the CVs of both bare $BiVO_4$ and drop-cast Ni/$BiVO_4$ possess an irreversible oxidative peak at 0.3 or 0.4 V vs. RHE, respectively, that is not present in the CVs obtained in comparison electrolyte. This is attributed to the oxidation of formate to CO_2, as this peak is also observed at a slightly higher potential of 0.4 V vs. RHE for drop-cast Ni/$BiVO_4$, but not with bare electrolyte, independent of the material used.

Many literature sources state a lower oxidation potential for this reaction at approximately -0.4 V vs. RHE[47-49], as CO_2 is a more stable compound from a thermodynamic point of view. This would intuitively lead to the suggestion that formate oxidation in the examined system should take place at less oxidative potentials already, however, several influences must be considered.

Firstly, in electrolyte formate does not occur in isolated form, but solvated in aqueous solution and therefore strongly interacting with the surrounding water molecules.[50] The polar formate ion is thermodynamically stabilised by this mechanism. Additionally, the decrease of chemical potential by dilution further adds to the thermodynamic stability of solvated formate.[23]

As shown by the presented CV data, electrode material can influence the oxidation potential, as it is depicted in Figure 15. The oxidation potential shifted to a higher potential for drop-cast Ni/$BiVO_4$ compared to bare $BiVO_4$. This is a consequence of different overvoltages for the same reaction on different material, which stems from different reaction kinetics, indicating that the reaction is more hindered on drop-cast Ni/$BiVO_4$ compared to bare $BiVO_4$.

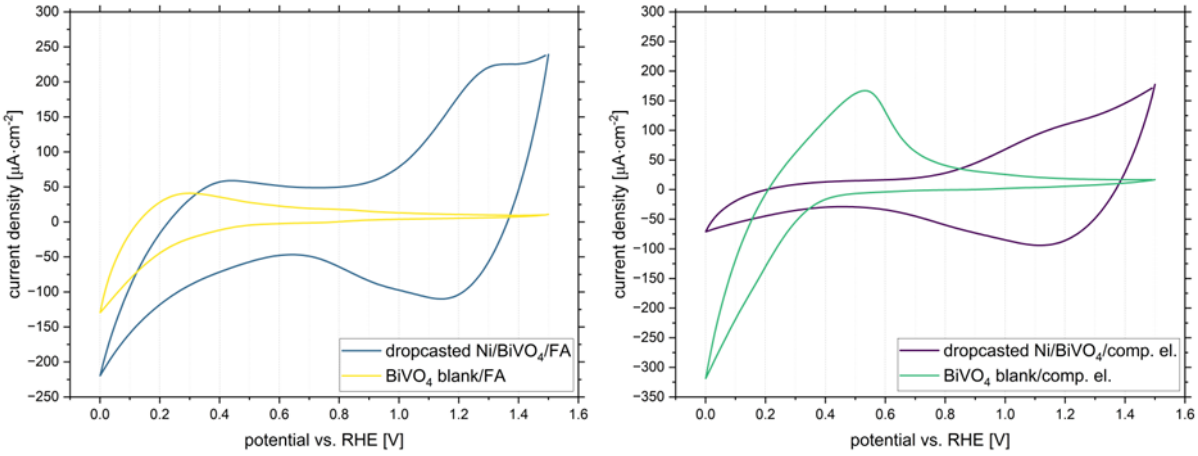

Figure 15: CV comparison of drop-cast Ni/$BiVO_4$ with bare $BiVO_4$; left: in FA electrolyte; right: in comparison electrolyte

In Figure 15 (left), a comparison between bare $BiVO_4$ and drop-cast Ni/$BiVO_4$ in FA electrolyte is provided. The most prominent difference is the capacitive behaviour of the sample with applied Ni, indicating lower conductivity of this material compared to the bare sample. At $E_{1/2}$ = 1.2 V, drop-cast Ni/$BiVO_4$ features a redox couple that can most likely be attributed to the redox reaction between Ni^{+2} and Ni^{+3}.[51] The oxygen evolution reaction could in theory also happen at a potential of 1.23 V, but since this would lead to a gaseous product leaving the electrolyte, the reductive peak is left to be unexplained by this. Furthermore, the OER usually presents at higher potentials due to the overpotential.

3.3.2.2 CV with light irradiation

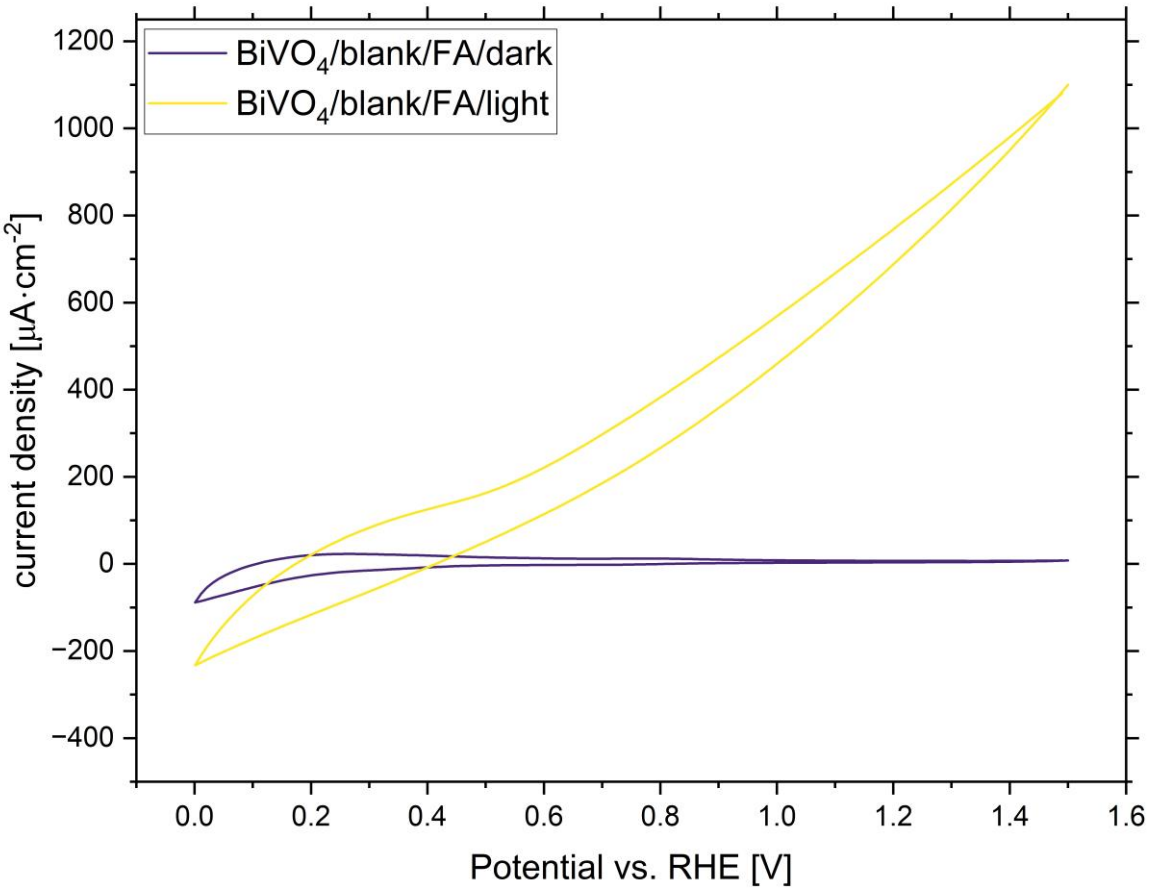

Figure 16: Comparison of cyclic voltammetry plots for bare $BiVO_4$ in FA electrolyte between light irradiation and no light irradiation

The main difference in CV plots in case of light irradiation, compared to CVs without light irradiation, is the clear behaviour as photoanode, as higher currents were measured at the same potential under light irradiation for all samples in all electrolytes. Representatively, this is shown for bare $BiVO_4$ in FA electrolyte in Figure 16.

3.3.3 Chronoamperometry

The focus of this thesis was the examination of drop-cast Ni/$BiVO_4$ from acetate precursor under photoelectrochemical conditions. To obtain reliable results, every combination of experimental condition was repeated three times. Bare $BiVO_4$ was examined both for gathering information on the potential of $BiVO_4$ itself towards selective formate oxidation as well as for comparison with samples loaded with co-catalysts to be able to tell if improvements were made by application of co-catalysts.

After assembly of the electrolysis cell, both half cells were purged with N_2 for 60 min to eliminate the oxygen in the headspace as well as the oxygen dissolved in the electrolyte. This

was done to tackle possible impact of oxygen on the reaction such as unwanted oxidation or radical induced reactions. The electrolysis lasted for 2 h at a voltage of 0.4 V vs. RHE.

For each electrolysis, a gas sample of both half cells of the H-cell was drawn before and after the reaction, leading to 4 injections in total per electrolysis. From the gas phase composition before and after every experiment, product generation rates in nmol·h^{-1} were calculated and from these, average values were calculated. Hereby, for CO_2 (K_B = 1670 bar)[32] also dissolved CO_2 in the electrolyte was considered by applying Henry's law (Equation 11). This was not performed for H_2 because of its low solubility in water.

Equation 11: Henry's law

$$p_B = x_B \cdot K_B$$

p_B … partial pressure of component B over the electrolyte
x_B … molar fraction of component B in solution
K_B … Henry's constant

Table 4 lists the calculated average product generation rates for CO_2 (half cell of the working electrode) and H_2 (half cell of the counter electrode) including standard deviation for all combinations of materials and electrolyte. In general, no CO was produced with any combination of material and electrolyte, indicating high selectivity towards FA dehydrogenation pathway. Measurements performed with FA electrolyte yielded significantly higher production rates for CO_2 and H_2 than measurements in comparison electrolyte, confirming that FA was the source for both products. For both materials, within the selected reaction time of 2 h, significantly higher product generation rates were achieved in comparison to the highest performing titania-based sample under photocatalytic conditions.

Table 4: Calculated average production rates of target products CO_2 and H_2 for every experimental condition

experimental condition	production rate CO_2 in nmol·h^{-1}	production rate H_2 in nmol·h^{-1}
bare $BiVO_4$ in comp. el.	138 ± 82	129 ± 131
bare $BiVO_4$ in FA el.	2669 ± 451	1281 ± 470
Ni/$BiVO_4$ in comp. el.	132 ± 24	248 ± 68
Ni/$BiVO_4$ in FA el.	2259 ± 2178	872 ± 163

In Figure 17 the data from Table 4 is depicted as a bar plot. On average, application of Ni co-catalyst led to reduced production rates for both products. Possibly, this is a consequence of the reduced conductivity of drop-cast Ni/$BiVO_4$ as indicated by the capacitive behaviour in cyclic voltammetry.

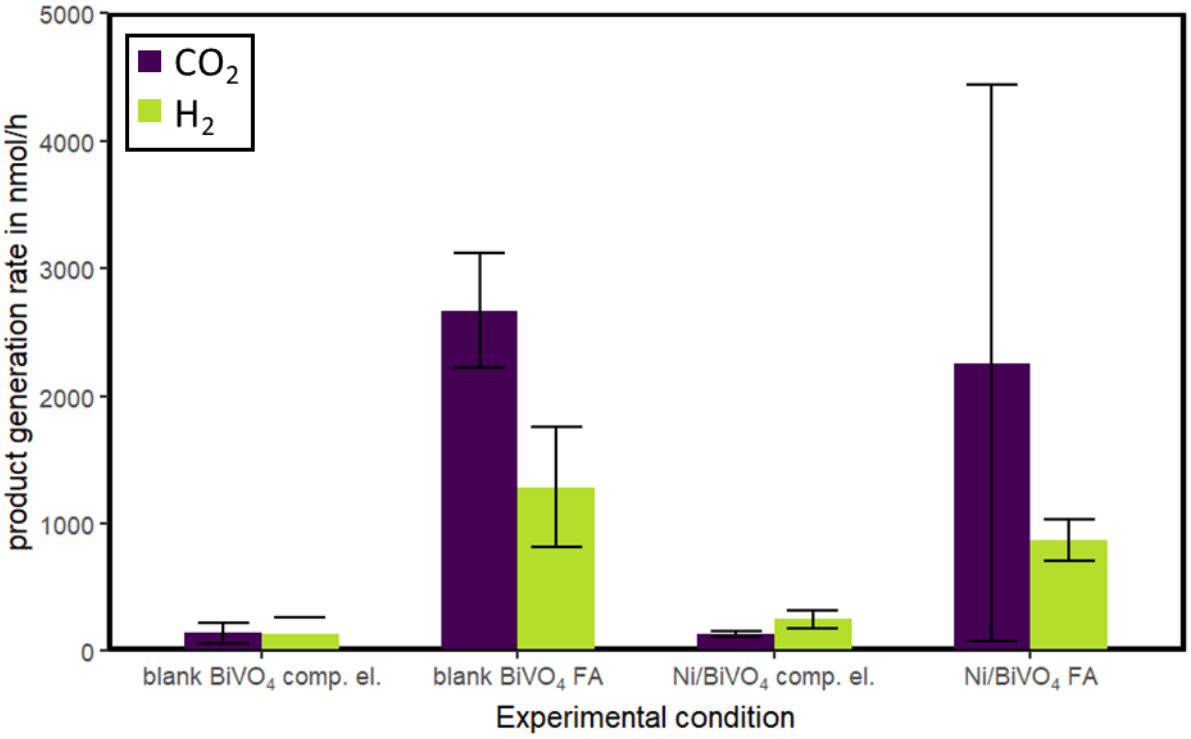

Figure 17: Comparison of average product generation rates between different experimental conditions using $BiVO_4$ under photoelectrochemical conditions

Additionally, there is a high standard deviation within measurements examining drop-cast $Ni/BiVO_4$ in FA electrolyte. This is a consequence of an outlier within the experimental outcomes of drop-cast $Ni/BiVO_4$ in FA electrolyte, that showed independently both in the GC analysis and the recordings of the potentiostat and that remains unexplained for now, as reactor, reference and counter electrode used were always the same. This renders a measurement error in gas detection and potentiostatic detection unlikely, as well as differing results due to differing equipment used. It is rather assumed that, despite electrodes from the same type always originating from the same synthesis batch, a difference in material interaction with the electrolyte is observed. A possible hint to an explanation is given by a recent publication utilizing a similar material combination (Ni nanoparticles on $BiVO_4$) for OER, where the in-situ formation of active Ni^{3+} was triggered by a pre-oxidation step.[52] Possibly, the oxidation Ni^{2+} to Ni^{3+} was in some cases triggered on the examined samples as well by preceding CV measurements before the electrolysis. Further examination of material behaviour is needed to explain this phenomenon.

3.4. Material stability

3.4.1 TiO_2-based material

Material stability for Ni-loaded TiO_2 samples Ti-08 and Ti-09 (0.05 and 1 µmol·cm^{-2}) was examined by comparison of XRD spectra before and after photoreaction. In Figure 18 a comparison between XRD spectra as synthesised (bottom) and after photoreaction (top) for Ti-08 (left) and Ti-09 (right) is presented. Both materials show changes in spectra after the photoreaction in the shape of additional peaks detected. The higher co-catalyst concentration on Ti-09 becomes apparent due to a broad Ni(200)[42] peak appearing after photoreaction that was not detected for Ti-08 after photoreaction. This possibly indicates a recrystalising process during the photoreaction of the drop-cast co-catalyst. On both samples, peaks (marked by *) were detected, that could not be matched to any reference data.

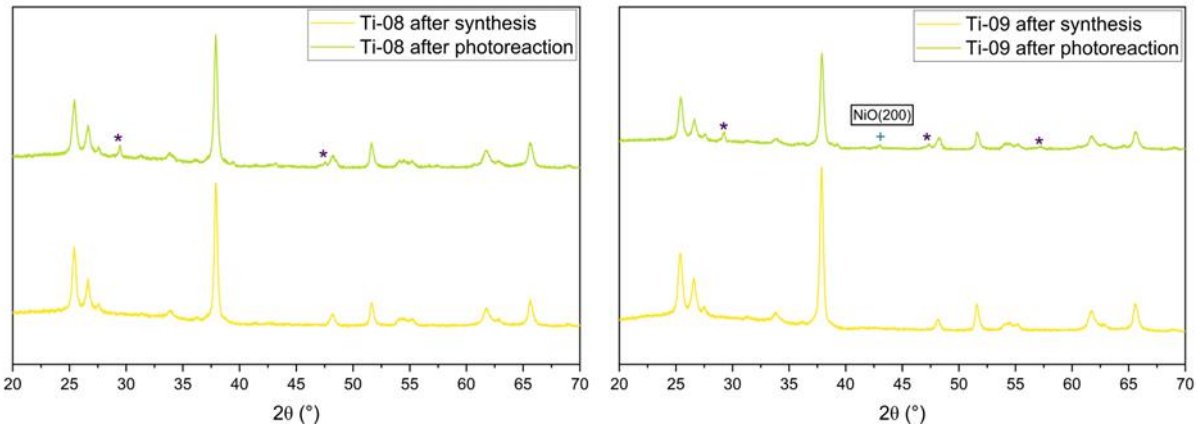

Figure 18: left: XRD spectra of Ti-08 as synthesised (bottom) and after photoreaction (top); right: XRD spectra of Ti-09 as synthesised (bottom) and after photoreaction (top)

3.4.2 $BiVO_4$-based material

Material stability was examined by conducting analysis methods XRD, SEM/EDX and XPS on selected samples after photocatalytic or photoelectrocatalytic tests. In Figure 19, XRD spectra are compared between pristine material, material after electrolysis in FA electrolyte and material after electrolysis in comparison electrolyte for bare $BiVO_4$ (left) and for drop-cast Ni/$BiVO_4$ (right). No change in XRD spectra was observed, indicating material stability over the examined electrolysis duration of 2 h.

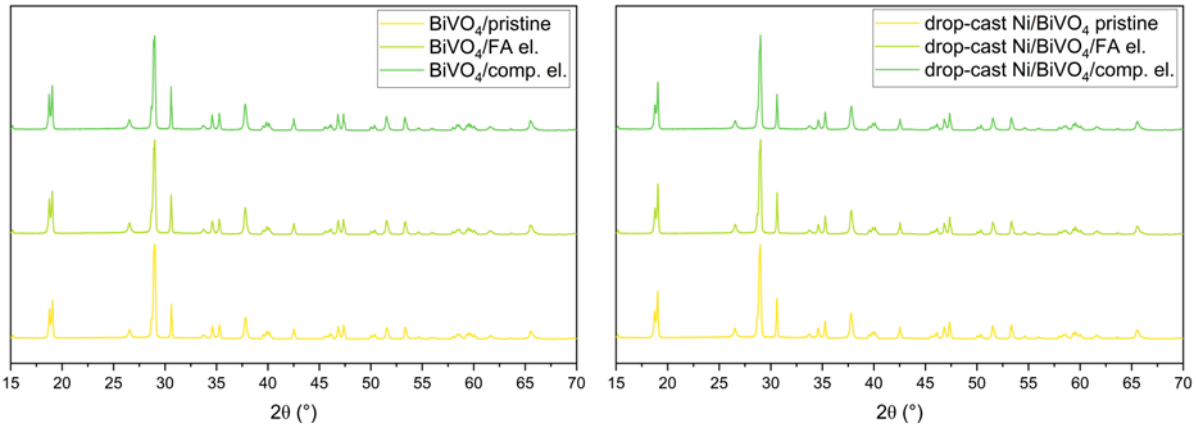

Figure 19: Comparison of XRD spectra as synthesised, after electrolysis in FA electrolyte and after electrolysis in comparison electrolyte; left: for bare $BiVO_4$; right: for drop-cast $Ni/BiVO_4$

In Figure 20 a detail of the comparison between diffraction spectra for bare $BiVO_4$ after synthesis and drop-cast $Ni/BiVO_4$ as synthesised, after electrolysis in comparison electrolyte and after electrolysis in FA electrolyte is presented. With all Ni-loaded samples showing congruent plots, the broad peaks indicating the presence of NiO as mentioned in 3.1.2.2 are still present after electrolysis which is an indication of the stability of the co-catalyst.

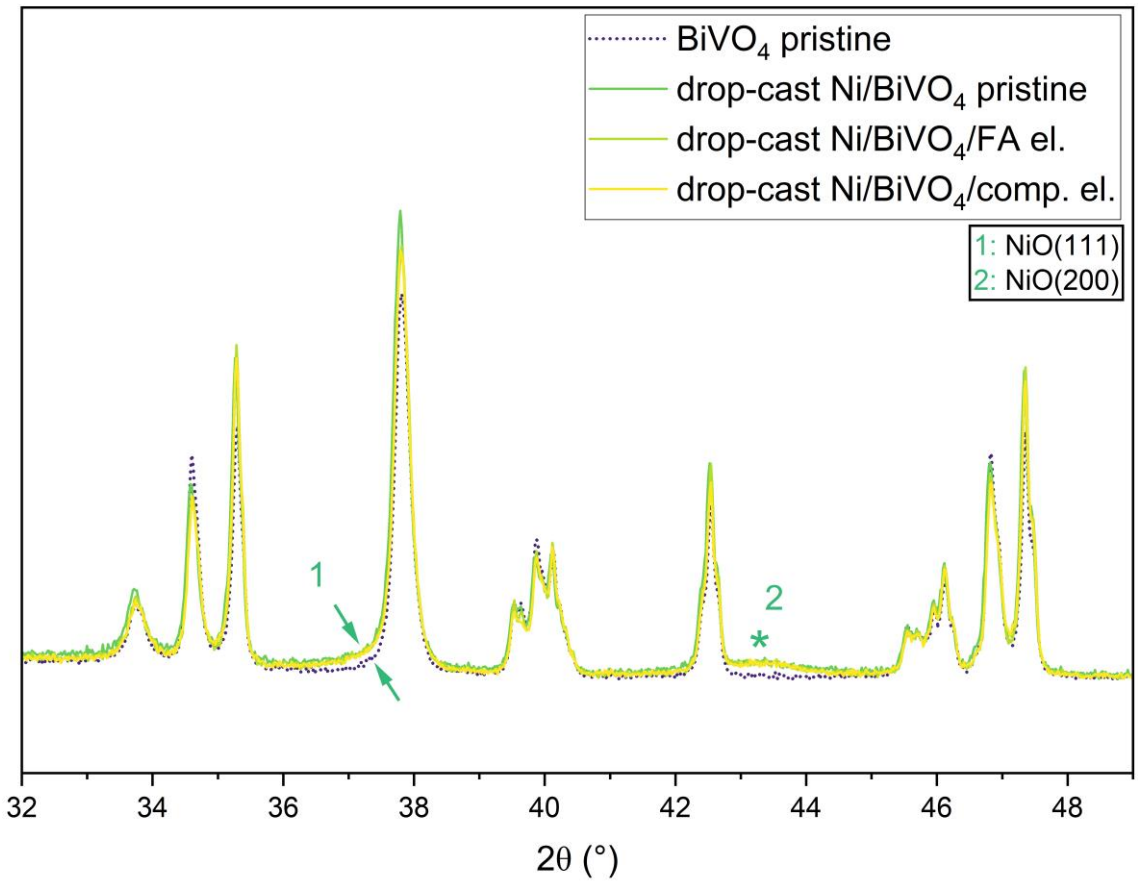

Figure 20: Overlay of XRD spectra for pristine bare $BiVO_4$, pristine drop-cast $Ni/BiVO_4$, drop-cast $Ni/BiVO_4$ after electrolysis in FA electrolyte and drop-cast $Ni/BiVO_4$ after electrolysis in comparison electrolyte

In Figure 22 a comparison between SEM images are depicted. Figure 22 A, C and E show the bare $BiVO_4$ sample as synthesised, after electrolysis in comparison electrolyte and after electrolysis in FA electrolyte, respectively. While the porous morpholgy was kept in FA electrolyte, the image of bare $BiVO_4$ after electrolysis in comparison electrolyte shows a collapse of the porous morphology, potentially leading to decreased surface area and therefore a decreased amount of active sites. Figure 22 B, D and F show the drop-cast Ni/$BiVO_4$ sample as synthesised, after electrolysis in comparison electrolyte and after electrolysis in FA electrolyte, respectively. After electrolysis in both electrolytes the Ni-rich bowl-shaped precipitates appeared more pronounced which is a possible indication of a re-structuring process during electrolysis.

A comparison of XPS survey spectra of the examined material as synthesised and after electrolysis in FA electrolyte is given in Figure 21 (left). Here, the increase of intensity of the C 1s peak is apparent, which is very likely a consequence of the exposure to the carbon containing reactant. A comparison between the detail of the Ni 2p signal of pristine drop-cast Ni/$BiVO_4$ and the same material after electrolysis is given in Figure 21 (right). While the general signal shape, containing the main signal between 856 and 853 eV and a satellite signal appearing at 861 eV, did not change during the electrolysis, the valley region in between was subjected to the growth of a peak at 857 eV. Possibly, this is the consequence of a change in Ni oxidation state to Ni^{3+}, as it has been observed before for a similar material combination (Ni nanoparticles on $BiVO_4$) under OER conditions, where the appearance of a shoulder peak at 857 eV is as well attributed to the presence of Ni^{3+}.[52] The theory, that this shoulder peak can be attributed to the presence of Ni^{3+} is supported by other publications as well.[53, 54]

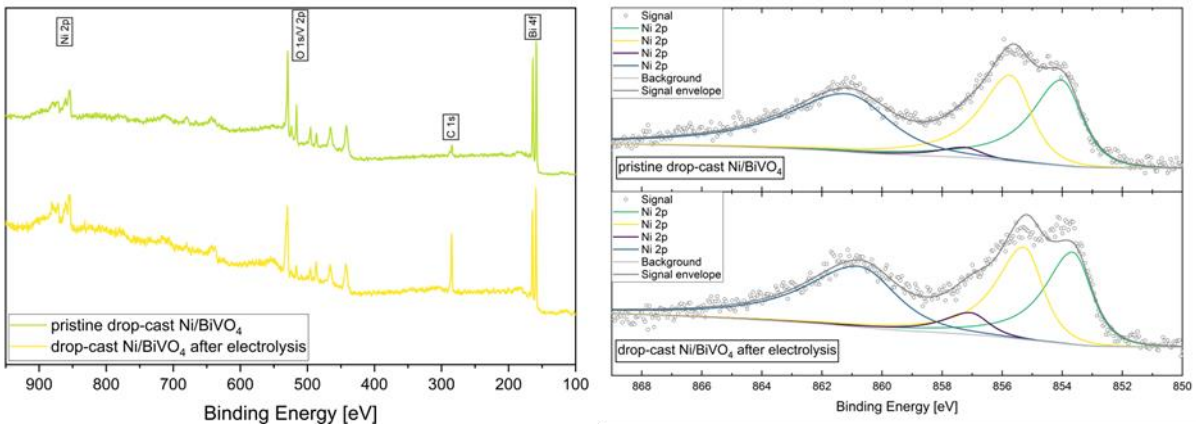

Figure 21: Comparison of XPS spectra between drop-cast Ni/BiVO4 as synthesised and after electrolysis in FA electrolyte; left: survey spectrum; right: detail of the area of Ni 2p signal

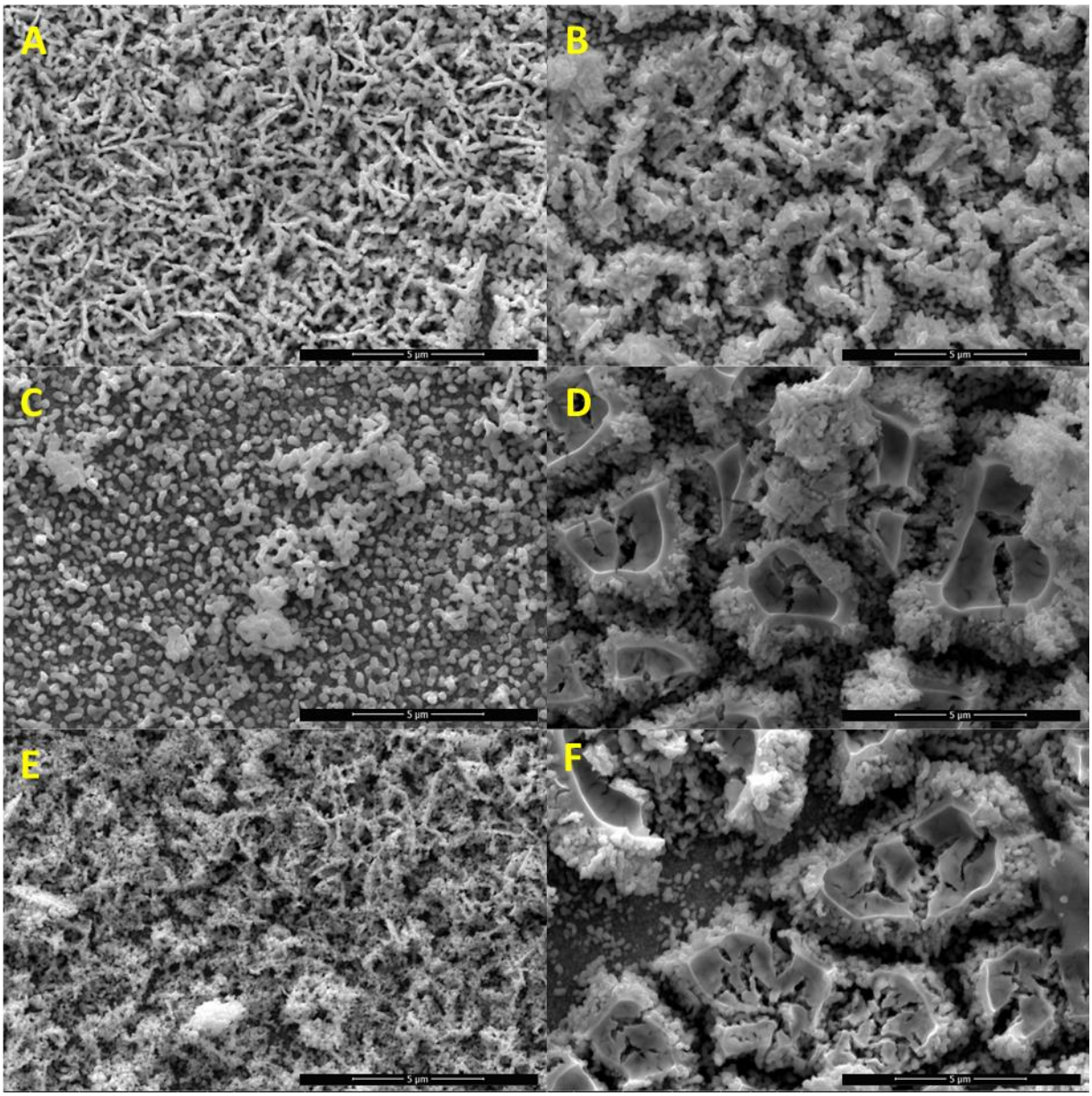

Figure 22: SEM images at a magnification of 20000; (A) pristine bare $BiVO_4$; (B) pristine drop-cast Ni/$BiVO_4$; (C) bare $BiVO_4$ after electrolysis in comparison electrolyte; (D) drop-cast Ni/$BiVO_4$ after electrolysis in comparison electrolyte; (E) bare $BiVO_4$ after electrolysis in FA electrolyte; (F) drop-cast Ni/$BiVO_4$ after electrolysis in FA electrolyte.

4. Conclusion

The scope of this thesis was to examine $BiVO_4$, a semiconductor with a bandgap in the visible light range that has recently gained attention for catalytic applications for oxygen evolution reaction, for its photocatalytic properties towards formic acid dehydrogenation. For this, preliminary photocatalytic experiments were conducted, examining Cu and Ni for their abilities to act as co-catalyst for the targeted reaction on TiO_2.

From several synthesis approaches, photodeposited Cu from acetate precursor and drop-cast Ni from acetate precursor showed interesting properties for catalysing the desired reaction under photocatalytic conditions on TiO_2. These two application methods for co-catalysts were therefore conducted on $BiVO_4$ to examine bare $BiVO_4$ and $BiVO_4$ with attached co-catalysts for their catalytic properties towards the dehydrogenation of formic acid.

Successful synthesis of porous monoclinic $BiVO_4$ as well as successful application of Ni as NiO by a simple drop-casting method was confirmed by means of X-ray powder diffraction (XRD), scanning electron microscopy in combination with energy dispersive X-ray analysis (SEM/EDX) and X-ray photoelectron spectroscopy (XPS).

The lower bandgap energy of the visible light photocatalyst was not sufficient to perform the desired reaction. It is assumed that the chemical potential of formic acid in aqueous solution is low and therefore hard to overcome, additional to possible kinetic barriers.

However, application of external potential allowed for raising the available oxidation potential. Under photoelectrocatalytic conditions it was confirmed that monoclinic $BiVO_4$ can act as a catalyst with absolute selectivity to the dehydrogenation of formic acid, which is important as the competing dehydration of formic acid is a highly undesired reaction for the application of the target compound hydrogen, as it produces CO. It was found that the reaction was higher yielding in electrolytes with a pH value over the pK_a of formic acid. This confirms that under electrocatalytic conditions, formate allows for higher reaction rates than formic acid.

Samples with applied Ni co-catalyst showed no favorable properties for the desired reaction in comparison with bare monoclinic $BiVO_4$ on average, however, under yet to be determined circumstances drastically higher yields were achieved. It is possible that in-situ generated Ni^{3+} plays a role in this activity change as a similar effect has been described before for a similar material used for oxygen evolution reaction (OER). Further studies on this behaviour are necessary.

Material stability was examined by comparing XRD, SEM/EDX and XPS measurements of the material after performed electrolysis with the same measurements performed on pristine samples. While monoclinic $BiVO_4$ proved to be stable under formic acid photoreforming, the samples with applied Ni co-catalyst showed a slight variation in Ni XPS signal after the electrolysis, indicating a change in oxidation state to Ni^{3+} which is a further hint towards catalytic activity of Ni^{2+}/Ni^{3+} redox couple in the desired reaction.

5. Acknowledgements

First and foremost, I thank Prof. Dominik Eder for the ability to be part of his research group and therefore to be able to learn, grow and hopefully become a better scientist. Thanks to his input I was able to understand what important qualities of a good scientific researcher are, which in his case not only include scientific knowledge, but also high interest in constructive discussions with all group members and being available for a friendly chat in between all of his appointments.

Furthermore, I thank 'Sherlock Ohms' Dr. Doğukan Apaydın, not only for introducing me to the topic of electrochemistry and CO_2 utilisation, but especially for being always available for questions, concerns and simple things like an afternoon coffee with the group or a proper dad joke. The latter quality should be especially highlighted, as throughout the past year he not only had to take care of questions and concerns by me and my colleagues in the group, but also of his new born child, which surely is a challenging combination of responsibilities that, from my point of view, he managed brilliantly.

A big thank you also goes out to the whole Eder research group. I always felt welcomed throughout the past months and whoever I approached with questions was always very happy to help. I want to express special thanks to Stephen Myakala for SEM/EDX measurements as well as to the other 'Dr. Wattsons' Jakob Blaschke for introducing me to working with $BiVO_4$, Hannah Rabl for XPS and SEM measurements and Dorottya Varga for sketching up two of the schemes I used in this thesis, being the most awesome lab baddie and more coffee/tea sessions than I should admit here.

Of course, I want to mention my family, not only the part here in Austria, but also everyone living in Bavaria and in Iraq. Due to my studies I have not always had time for you, and often I had to leave our gatherings early to study for the next exam or finish a report with an uncomfortably close deadline. At no point anyone questioned this, or tried to downplay the actual workload I had during the past years, despite often being invisble, especially to people who never had the opportunity to go to university. You simply believed me and believed in me and for that I want to express a warm and wholehearted Thank You!/شكراً جزيلاً لكم!

Last, but most certainly not least I want to thank my partner Verena who has been such an important part of my life throughout the last five years. Often I had late night study sessions and way too little time for leisure activities but still you've always been nothing but supportive and simply there for me when I needed you and for that I am grateful.

6. References

1. Usman, M. R., Hydrogen storage methods: Review and current status. *Renewable and Sustainable Energy Reviews* **2022,** *167*, 112743.
2. Wang, X.; Meng, Q.; Gao, L.; Jin, Z.; Ge, J.; Liu, C.; Xing, W., Recent progress in hydrogen production from formic acid decomposition. *International Journal of Hydrogen Energy* **2018,** *43*, 7055-7071.
3. Wang, A.; He, P.; Wu, J.; Chen, N.; Pan, C.; Shi, E.; Jia, H.; Hu, T.; He, K.; Cai, Q., Reviews on Homogeneous and Heterogeneous Catalysts for Dehydrogenation and Recycling of Formic Acid: Progress and Perspectives. *Energy & Fuels* **2023,** *37*, 17075-17093.
4. Pellegrino, F.; Sordello, F.; Mino, L.; Minero, C.; Hodoroaba, V.-D.; Martra, G.; Maurino, V., Formic acid photoreforming for hydrogen production on shape-controlled anatase TiO2 nanoparticles: assessment of the role of fluorides,{101}/{001} surfaces ratio, and platinization. *ACS Catalysis* **2019,** *9*, 6692-6697.
5. Li, L.; Guo, W.; Zhu, Y.; Wu, Y., Hydrogen production by photoelectrochemically splitting solutions of formic acid. *ChemSusChem* **2011,** *4*, 1475-1480.
6. Reichert, R.; Jusys, Z.; Behm, R. J., A novel photoelectrochemical flow cell with online mass spectrometric detection: oxidation of formic acid on a nanocrystalline TiO 2 electrode. *Physical Chemistry Chemical Physics* **2014,** *16*, 25076-25080.
7. He, C.; Li, X.; Xiong, Y.; Zhu, X.; Liu, S., The enhanced PC and PEC oxidation of formic acid in aqueous solution using a Cu–TiO2/ITO film. *Chemosphere* **2005,** *58*, 381-389.
8. Park, Y.; McDonald, K. J.; Choi, K.-S., Progress in bismuth vanadate photoanodes for use in solar water oxidation. *Chemical Society Reviews* **2013,** *42*, 2321-2337.
9. Tayebi, M.; Tayyebi, A.; Lee, B.-K., Photocharged molybdenum-doped BiVO4 photoanodes for simultaneous enhancements in charge transport and surface passivation. *Solar Energy* **2019,** *191*, 427-434.
10. Tayebi, M.; Lee, B.-K., The effects of W/Mo-co-doped BiVO4 photoanodes for improving photoelectrochemical water splitting performance. *Catalysis Today* **2021,** *361*, 183-190.
11. Rifkin, J., *The hydrogen economy*. Penguin2003.
12. Bockris, J. O. M., A hydrogen economy. *Science* **1972,** *176*, 1323-1323.
13. van Renssen, S., The hydrogen solution? *Nature Climate Change* **2020,** *10*, 799-801.
14. Parkes, R. Toyota unveils its first new hydrogen car in a decade, to go on sale this autumn https://www.hydrogeninsight.com/transport/toyota-unveils-its-first-new-hydrogen-car-in-a-decade-to-go-on-sale-this-autumn/2-1-1433307 (15.01.2024),
15. Atilhan, S.; Park, S.; El-Halwagi, M. M.; Atilhan, M.; Moore, M.; Nielsen, R. B., Green hydrogen as an alternative fuel for the shipping industry. *Current Opinion in Chemical Engineering* **2021,** *31*, 100668.
16. Newborough, M.; Cooley, G., Developments in the global hydrogen market: The spectrum of hydrogen colours. *Fuel Cells Bulletin* **2020,** *2020*, 16-22.
17. Harmsen, M.; van Vuuren, D. P.; Bodirsky, B. L.; Chateau, J.; Durand-Lasserve, O.; Drouet, L.; Fricko, O.; Fujimori, S.; Gernaat, D. E.; Hanaoka, T., The role of methane in future climate strategies: mitigation potentials and climate impacts. *Climatic Change* **2020,** *163*, 1409-1425.

18. Squadrito, G.; Maggio, G.; Nicita, A., The green hydrogen revolution. *Renewable Energy* **2023,** *216*, 119041.
19. Klopčič, N.; Grimmer, I.; Winkler, F.; Sartory, M.; Trattner, A., A review on metal hydride materials for hydrogen storage. *Journal of Energy Storage* **2023,** *72*, 108456.
20. Lai, Q.; Pratthana, C.; Yang, Y.; Rawal, A.; Aguey-Zinsou, K.-F., Nanoconfinement of complex borohydrides for hydrogen storage. *ACS Applied Nano Materials* **2021,** *4*, 973-978.
21. Liu, M.; Xu, Y.; Meng, Y.; Wang, L.; Wang, H.; Huang, Y.; Onishi, N.; Wang, L.; Fan, Z.; Himeda, Y., Heterogeneous catalysis for carbon dioxide mediated hydrogen storage technology based on formic acid. *Advanced Energy Materials* **2022,** *12*, 2200817.
22. Fang, M.; Tan, X.; Liu, Z.; Hu, B.; Wang, X., Recent Progress on Metal-Enhanced Photocatalysis: A Review on the Mechanism. *Research* **2021,** *2021*.
23. Wedler, G.; Freund, H.-J., *Lehr-und arbeitsbuch physikalische chemie*. John Wiley & Sons2019.
24. Iqbal, M., *An introduction to solar radiation*. Elsevier2012.
25. Mortimer, C. E.; Müller, U., Das Basiswissen der Chemie. *Stuttgart, New York* **2003,** *122015*, 103.
26. Kumaravel, V.; Pillai, S. C., *Photocatalysis*. De Gruyter: Berlin, Germany

Boston, Massachusetts :, 2021; p 1 online resource (396 pages).
27. Peiris, S.; de Silva, H. B.; Ranasinghe, K. N.; Bandara, S. V.; Perera, I. R., Recent development and future prospects of TiO2 photocatalysis. *Journal of the Chinese Chemical Society* **2021,** *68*, 738-769.
28. Humayun, M.; Raziq, F.; Khan, A.; Luo, W., Modification strategies of TiO2 for potential applications in photocatalysis: a critical review. *Green Chemistry Letters and Reviews* **2018,** *11*, 86-102.
29. Candal, R. J.; Zeltner, W. A.; Anderson, M. A., Effects of pH and applied potential on photocurrent and oxidation rate of saline solutions of formic acid in a photoelectrocatalytic reactor. *Environmental science & technology* **2000,** *34*, 3443-3451.
30. Trinh, D. T. T.; Khanitchaidecha, W.; Channei, D.; Nakaruk, A., Synthesis, characterization and environmental applications of bismuth vanadate. *Research on Chemical Intermediates* **2019,** *45*, 5217-5259.
31. Chorkendorff, I.; Niemantsverdriet, J. W., *Concepts of modern catalysis and kinetics*. John Wiley & Sons2017.
32. Atkins, P. W.; De Paula, J., *Physikalische chemie*. John Wiley & Sons2013.
33. Haselmann, G. M. TiO2-based photocatalysis: role of defects during photocatalytic hydrogen evolution and oxidation of methanol. Technische Universität Wien2018.
34. Kim, T. W.; Choi, K.-S., Nanoporous BiVO4 photoanodes with dual-layer oxygen evolution catalysts for solar water splitting. *Science* **2014,** *343*, 990-994.
35. Spieß, L.; Teichert, G.; Schwarzer, R.; Behnken, H.; Genzel, C., *Moderne Röntgenbeugung : Röntgendiffraktometrie für Materialwissenschaftler, Physiker und Chemiker*. 3. Aufl. 2019. ed.; Springer Fachmedien Wiesbaden Imprint: Springer Spektrum: Wiesbaden, 2019; p 1 Online-Ressource (XVI, 636 Seiten), 392 Illustrationen.
36. Vernon-Parry, K. D., Scanning electron microscopy: an introduction. *III-Vs review* **2000,** *13*, 40-44.
37. Watts, J. F.; Wolstenholme, J., *An introduction to surface analysis by XPS and AES*. John Wiley & Sons2019.

38. Elgrishi, N.; Rountree, K. J.; McCarthy, B. D.; Rountree, E. S.; Eisenhart, T. T.; Dempsey, J. L., A practical beginner's guide to cyclic voltammetry. *Journal of chemical education* **2018,** *95*, 197-206.
39. Thamaphat, K.; Limsuwan, P.; Ngotawornchai, B., Phase characterization of TiO2 powder by XRD and TEM. *Agriculture and Natural Resources* **2008,** *42*, 357-361.
40. Seki, H.; Ishizawa, N.; Mizutani, N.; Kato, M. In *High Temperature Structures of the Rutile-Type Oxides, TiO~2~ and SnO~2~*1984.
41. Sleight, A.; Chen, H.-Y.; Ferretti, A.; Cox, D., Crystal growth and structure of BiVO4. *Materials Research Bulletin* **1979,** *14*, 1571-1581.
42. Teoh, L. G.; Li, K.-D., Synthesis and characterization of NiO nanoparticles by sol–gel method. *Materials transactions* **2012,** *53*, 2135-2140.
43. Grosvenor, A. P.; Biesinger, M. C.; Smart, R. S. C.; McIntyre, N. S., New interpretations of XPS spectra of nickel metal and oxides. *Surface science* **2006,** *600*, 1771-1779.
44. Hori, Y.; Wakebe, H.; Tsukamoto, T.; Koga, O., Electrocatalytic process of CO selectivity in electrochemical reduction of CO2 at metal electrodes in aqueous media. *Electrochimica Acta* **1994,** *39*, 1833-1839.
45. Smith, R. M.; Martell, A. E., *Critical stability constants: second supplement*. Springer1989; Vol. 6.
46. ionic strength. 3.0.1 ed.; International Union of Pure and Applied Chemistry (IUPAC)2019.
47. RUSCHING, U.; MÜLLER, U.; WILLNOW, P.; HÖPNER, T., CO2 reduction to formate by NADH catalysed by formate dehydrogenase from Pseudomonas oxalaticus. *European Journal of Biochemistry* **1976,** *70*, 325-330.
48. Bassegoda, A.; Madden, C.; Wakerley, D. W.; Reisner, E.; Hirst, J., Reversible interconversion of CO2 and formate by a molybdenum-containing formate dehydrogenase. *Journal of the American Chemical Society* **2014,** *136*, 15473-15476.
49. Han, N.; Ding, P.; He, L.; Li, Y.; Li, Y., Promises of main group metal–based nanostructured materials for electrochemical CO2 reduction to formate. *Advanced Energy Materials* **2020,** *10*, 1902338.
50. Bruice, P. Y., *Organic chemistry*. Pearson2017.
51. Seghiouer, A.; Chevalet, J.; Barhoun, A.; Lantelme, F., Electrochemical oxidation of nickel in alkaline solutions: a voltammetric study and modelling. *Journal of Electroanalytical Chemistry* **1998,** *442*, 113-123.
52. Wen, P.; Lei, R.; Cao, X.; Ma, Q.; Zhang, G.; Guo, C.; Wang, X.; Qiu, Y., Anchored Ni nanocrystals boosting BiVO4 photoanode for highly efficient water oxidation via in-situ generation of Ni@ NiOOH co-catalyst. *Chemical Engineering Journal* **2023,** *454*, 139983.
53. Rathore, D.; Sharma, M. D.; Sharma, A.; Basu, M.; Pande, S., Aggregates of Ni/Ni(OH)2/NiOOH Nanoworms on Carbon Cloth for Electrocatalytic Hydrogen Evolution. *Langmuir* **2020,** *36*, 14019-14030.
54. Yi, L.; Niu, Y.; Feng, B.; Zhao, M.; Hu, W., Simultaneous phase transformation and doping via a unique photochemical–electrochemical strategy to achieve a highly active Fe-doped Ni oxyhydroxide oxygen evolution catalyst. *Journal of Materials Chemistry A* **2021,** *9*, 4213-4220.

7. Appendix

7.1. List of abbreviations

CA … chronoamperometry
CB … conduction band
CE … counter electrode
CV … cyclic voltammetry
DI … de-ionised
DMSO … di-methyl sulfoxide
$E_{1/2}$ … experimentally available potential of a redox-reaction
e^- … electron
E_B … bandgap
EDX … energy dispersive X-ray spectroscopy
E_F … fermi-Level
EtOH … ethanol
FA … formic acid
FTO … fluorine-doped tin oxide
h^+ … electron vacancy/hole
LOHC … liquid organic hydrogen carrier
LSV … linear sweep voltammetry
OER … oxygen evolution reaction
RE … reference electrode
RHE … reversible hydrogen electrode
SEM … scanning electron microscopy
UV … ultraviolet
VB … valence band
WE … working electrode
XPS … X-ray photoelectron spectroscopy
XRD … X-ray diffraction

7.2. List of Figures and Schemes

7.3. List of Tables

7.4. EDX data

7.4.1 Pristine bare $BiVO_4$

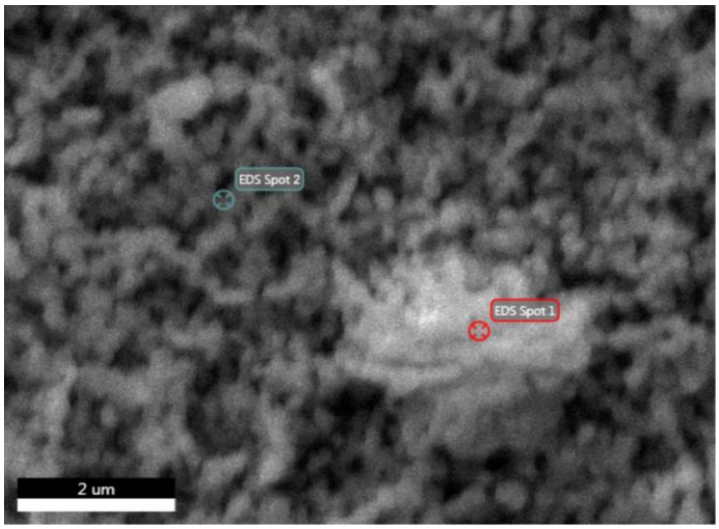

pristine bare $BiVO_4$ – Spot 1		
Element	Weight %	Atomic %
C K	11.4	35.3
O K	18.5	43.1
BiM	50.3	9.0
SnL	4.6	1.4
V K	15.4	11.3

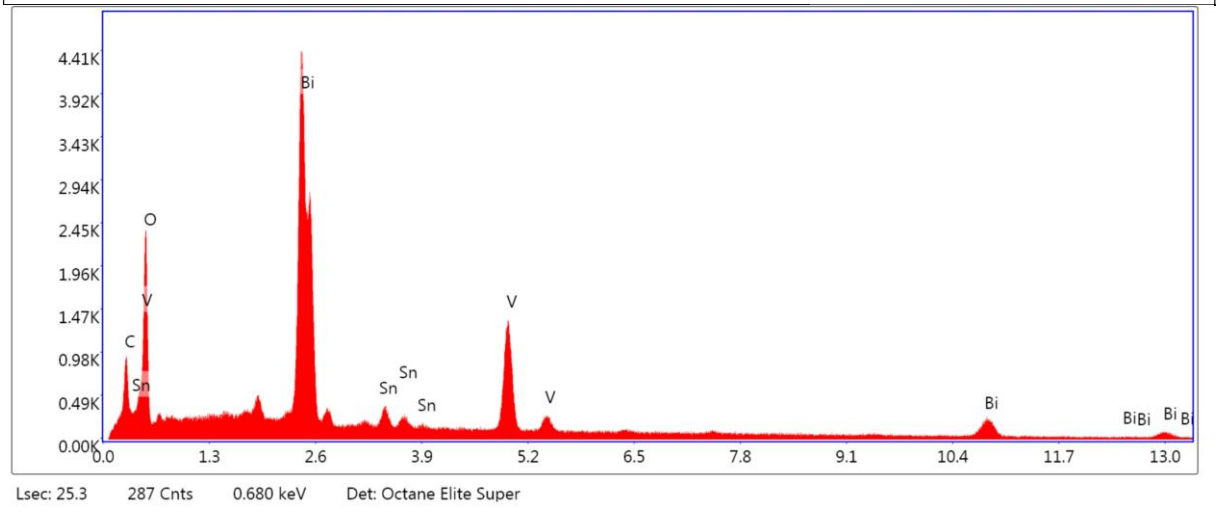

bare $BiVO_4$ – comp. el. – Spot 2

Element	Weight %	Atomic %
C K	8.0	30.8
O K	12.6	36.1
SiK	1.8	2.9
BiM	35.5	7.8
SnL	30.2	11.7
V K	12.0	10.8

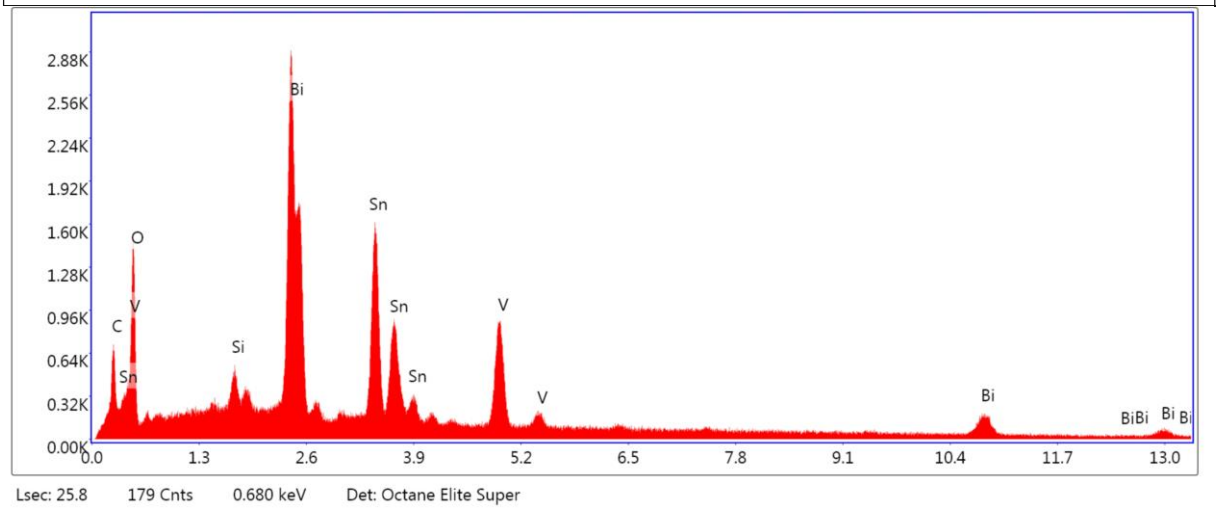

7.4.2 Bare $BiVO_4$ after electrolysis in comparison electrolyte

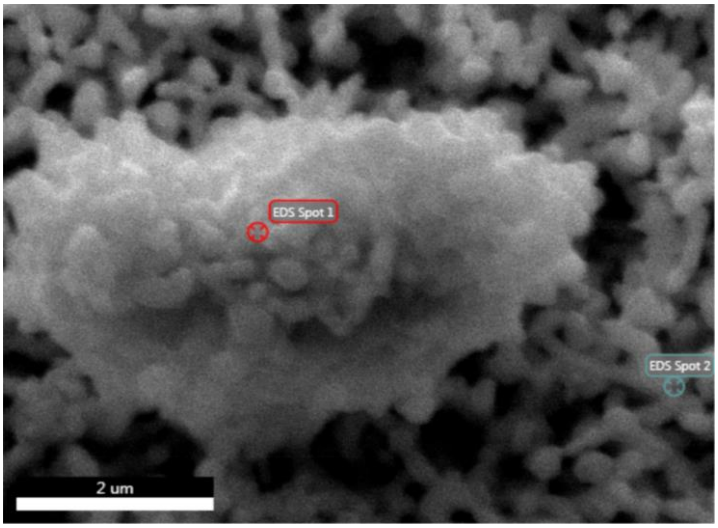

bare $BiVO_4$ – comp. el. – Spot 1		
Element	Weight %	Atomic %
C K	7.9	35.0
O K	8.2	27.2
SiK	0.4	0.7
BiM	63.2	16.0
V K	20.3	21.1

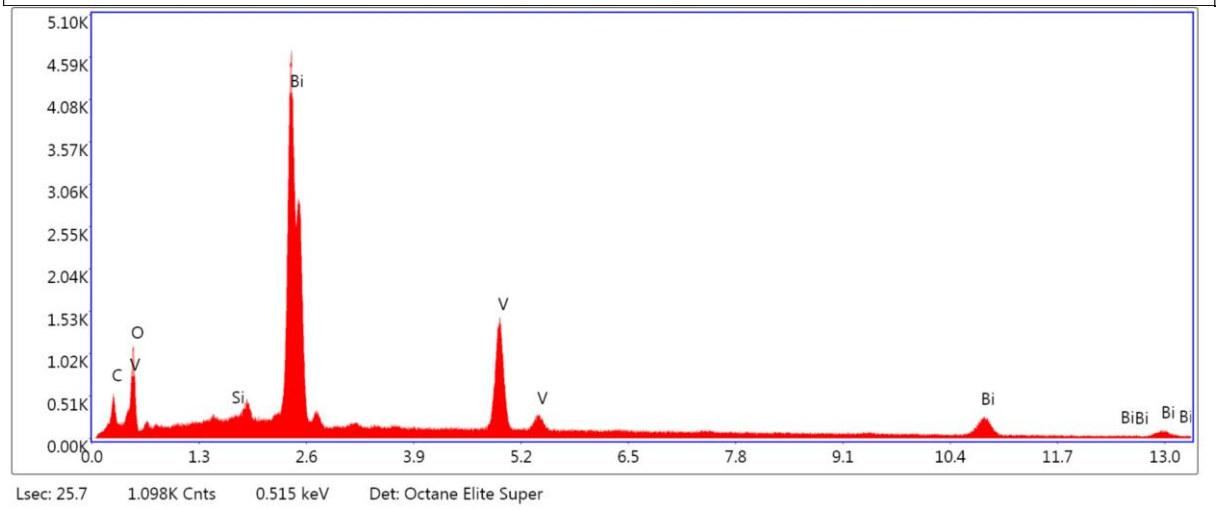

bare $BiVO_4$ – comp. el. – Spot 2		
Element	Weight %	Atomic %
C K	9.5	31.2
O K	18.0	44.4
SiK	0.4	0.6
BiM	45.4	8.6
SnL	12.5	4.2
V K	14.3	11.1

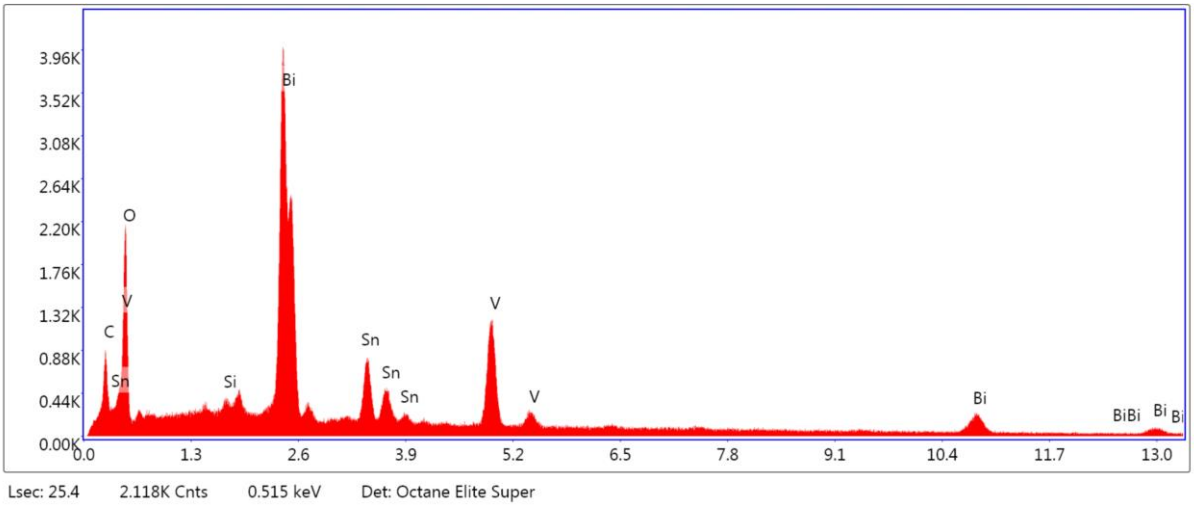

7.4.3 Bare $BiVO_4$ after electrolysis in FA electrolyte

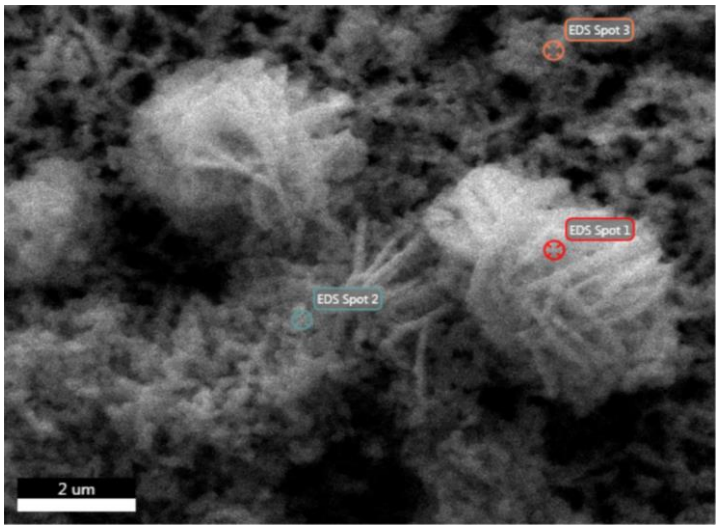

bare $BiVO_4$ – FA el. – Spot 1		
Element	Weight %	Atomic %
C K	11.9	39.0
O K	15.1	37.2
SiK	0.2	0.3
BiM	56.1	10.6
V K	16.6	12.9

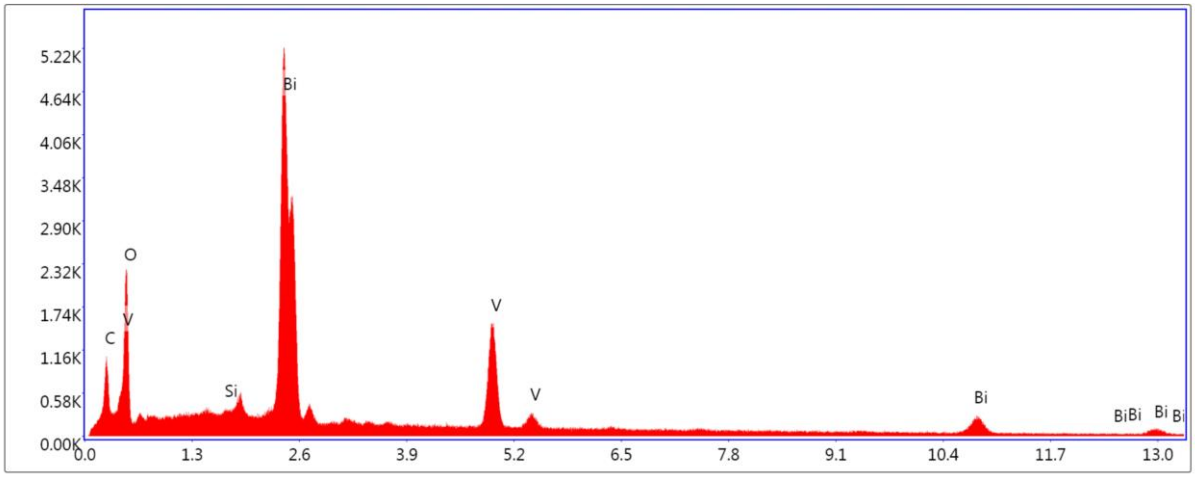

bare $BiVO_4$ – FA el. – Spot 2		
Element	Weight %	Atomic %
C K	11.3	37.1
O K	15.7	38.7
SiK	0.2	0.3
BiM	55.6	10.5
V K	17.2	13.4

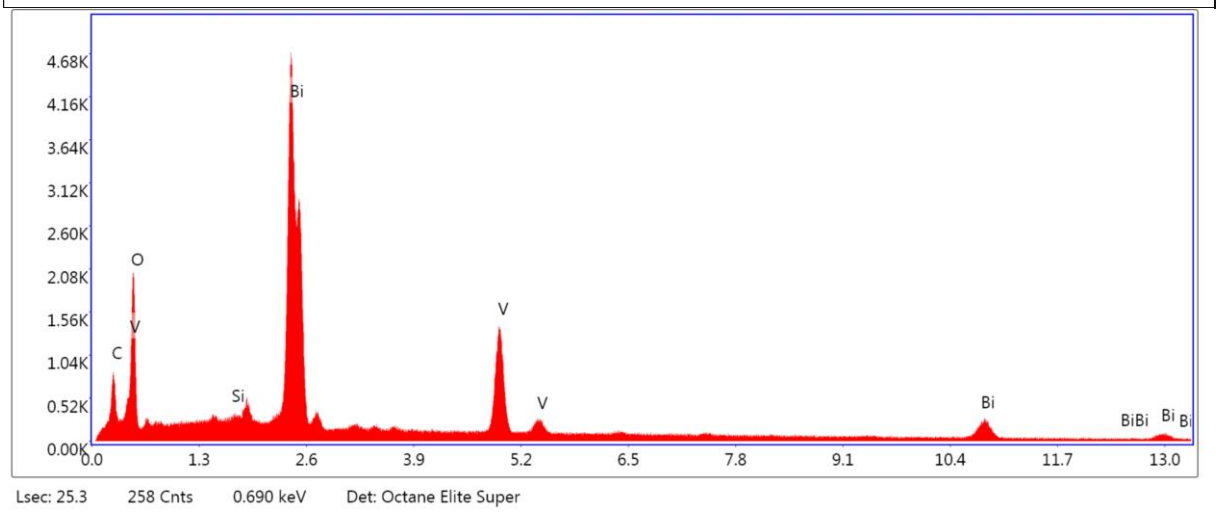

bare $BiVO_4$ – FA el. – Spot 3		
Element	Weight %	Atomic %
C K	8.8	32.2
O K	14.3	39.3
SiK	0.4	0.6
BiM	51.4	10.8
SnL	9.0	3.3
V K	16.1	13.9

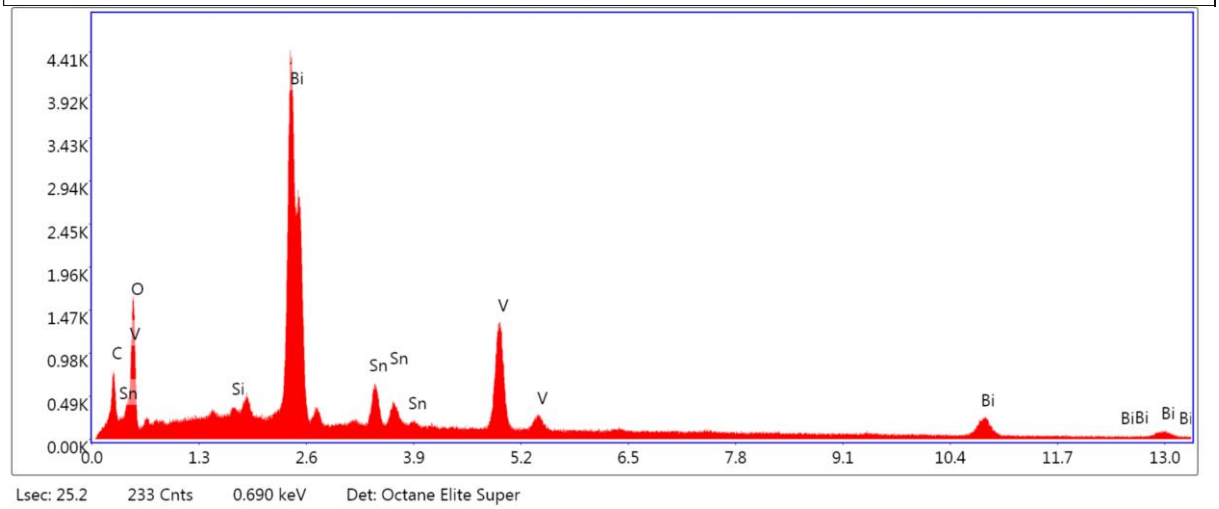

7.4.4 Pristine drop-cast Ni/$BiVO_4$

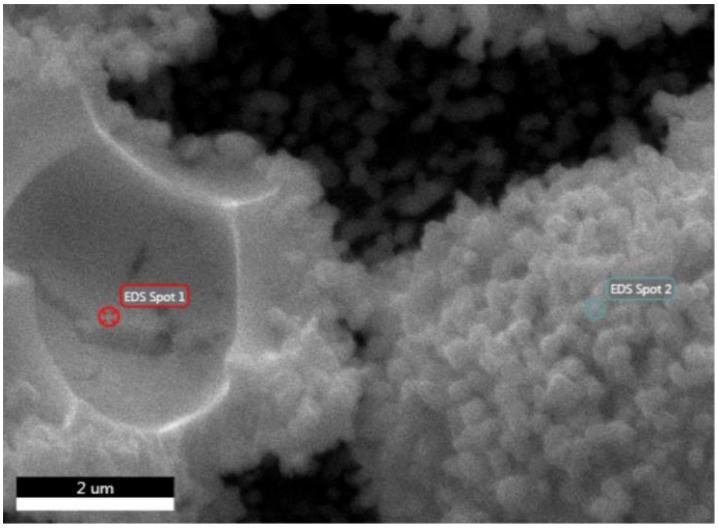

pristine drop-cast Ni/$BiVO_4$ – Spot 1		
Element	Weight %	Atomic %
O K	31.8	67.6
SiK	0.1	0.1
BiM	15.7	2.6
SnL	3.8	1.1
V K	5.0	3.4
NiK	43.5	25.2

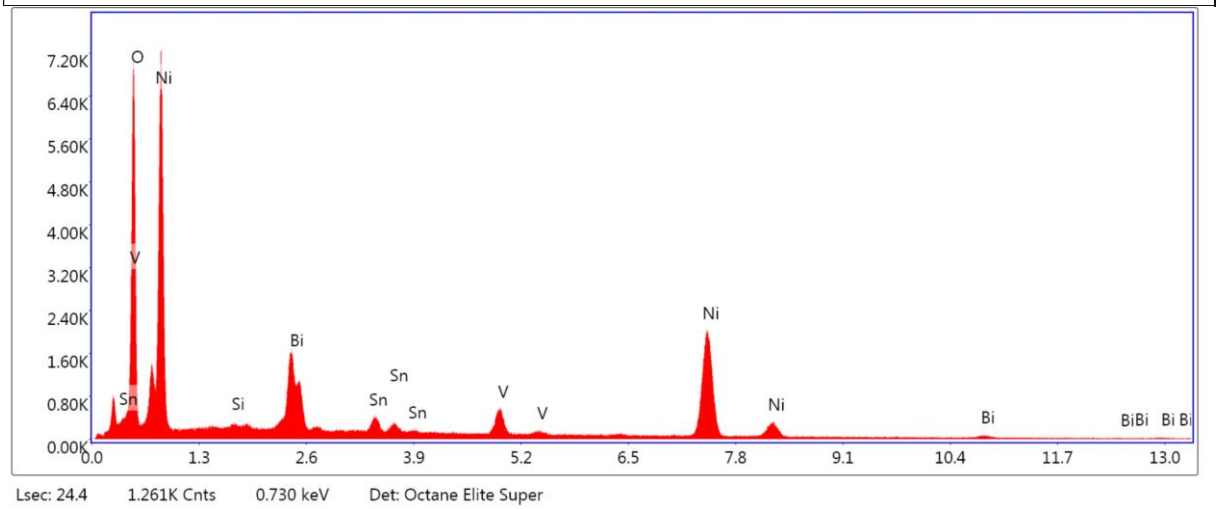

pristine drop-cast Ni/$BiVO_4$ – Spot 2		
Element	Weight %	Atomic %
C K	13.6	37.1
O K	19.5	39.7
SiK	0.1	0.1
BiM	37.6	5.9
V K	12.0	7.7
NiK	17.2	9.6

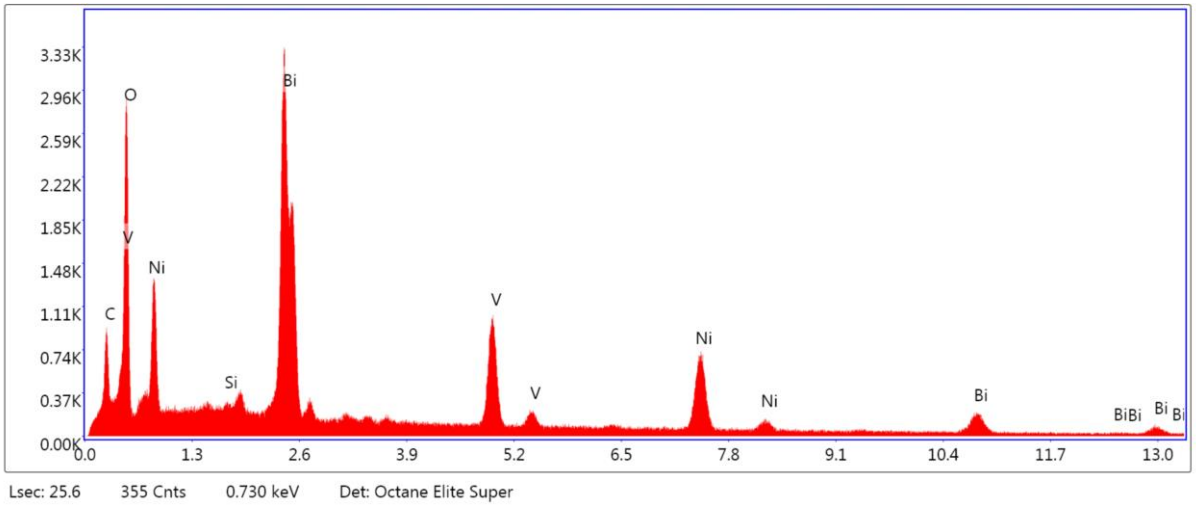

7.4.5 Drop-cast Ni/$BiVO_4$ after electrolysis in comparison electrolyte

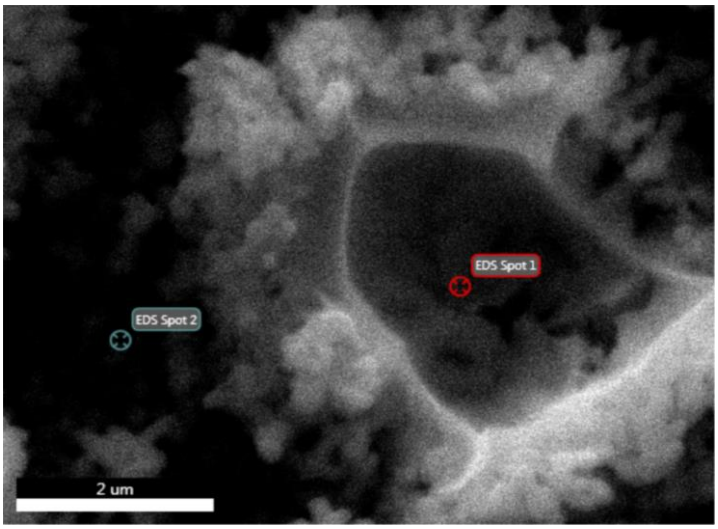

drop-cast Ni/$BiVO_4$ – comp. el. – Spot 1		
Element	Weight %	Atomic %
O K	25.7	64.7
BiM	29.6	5.7
SnL	5.9	2.0
V K	9.9	7.8
NiK	28.9	19.8

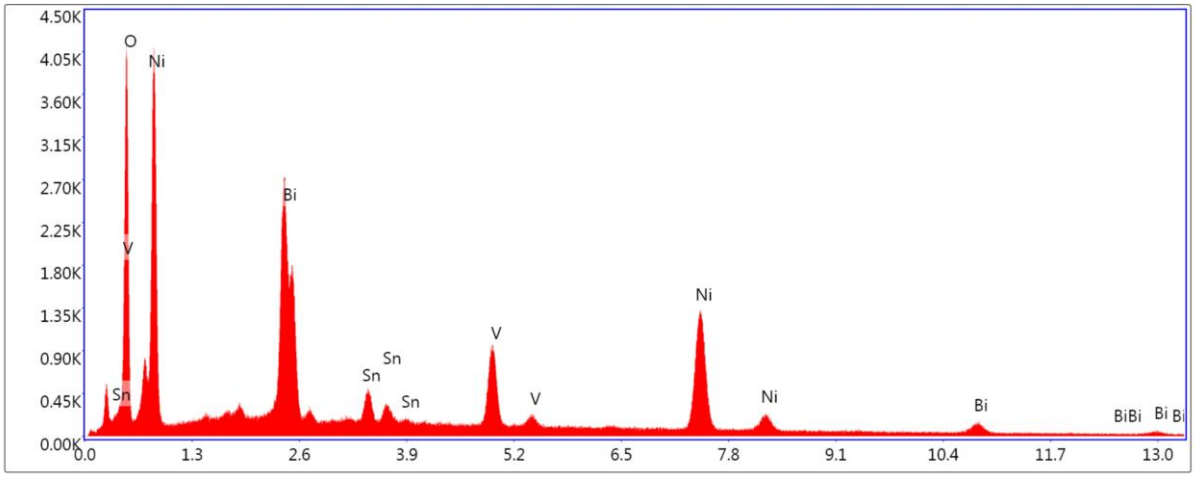

drop-cast Ni/$BiVO_4$ – comp. el. – Spot 2		
Element	Weight %	Atomic %
O K	6.2	29.2
SiK	3.1	8.4
BiM	23.8	8.5
SnL	51.4	32.5
V K	8.7	12.8
NiK	6.8	8.7

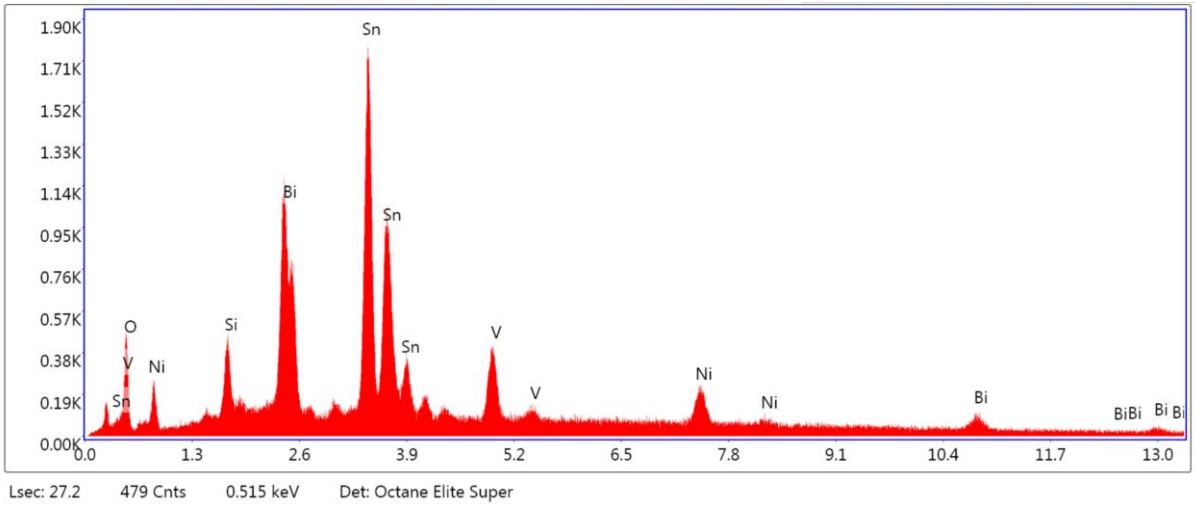

7.4.6 Drop-cast Ni/$BiVO_4$ after electrolysis in FA electrolyte

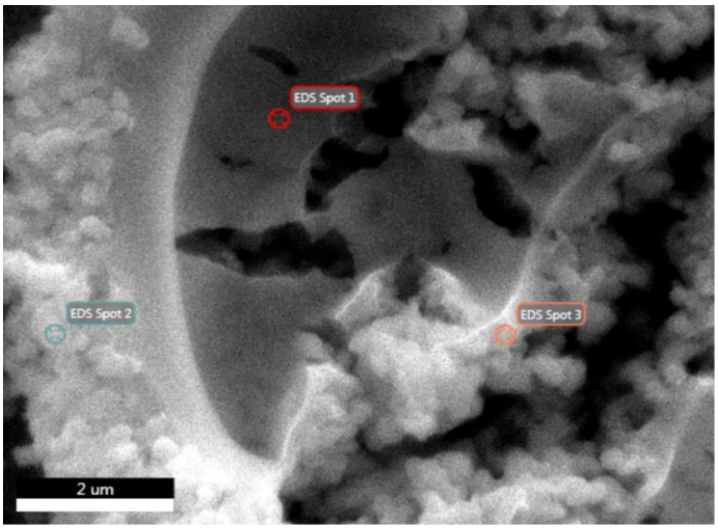

drop-cast Ni/$BiVO_4$ – FA el. – Spot 1		
Element	Weight %	Atomic %
O K	26.0	61.3
SiK	0.2	0.3
BiM	18.8	3.4
SnL	3.6	1.2
V K	7.8	5.8
NiK	43.6	28.1

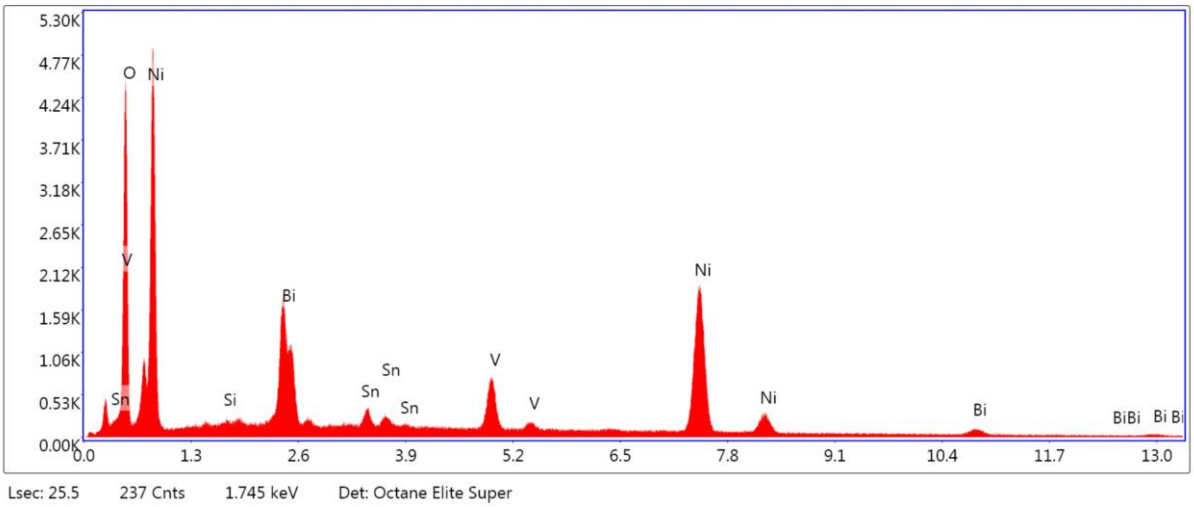

drop-cast Ni/$BiVO_4$ – FA el. – Spot 2		
Element	Weight %	Atomic %
O K	30.0	70.8
SiK	0.4	0.5
BiM	30.9	5.6
SnL	8.6	2.7
V K	10.4	7.7
NiK	19.7	12.6

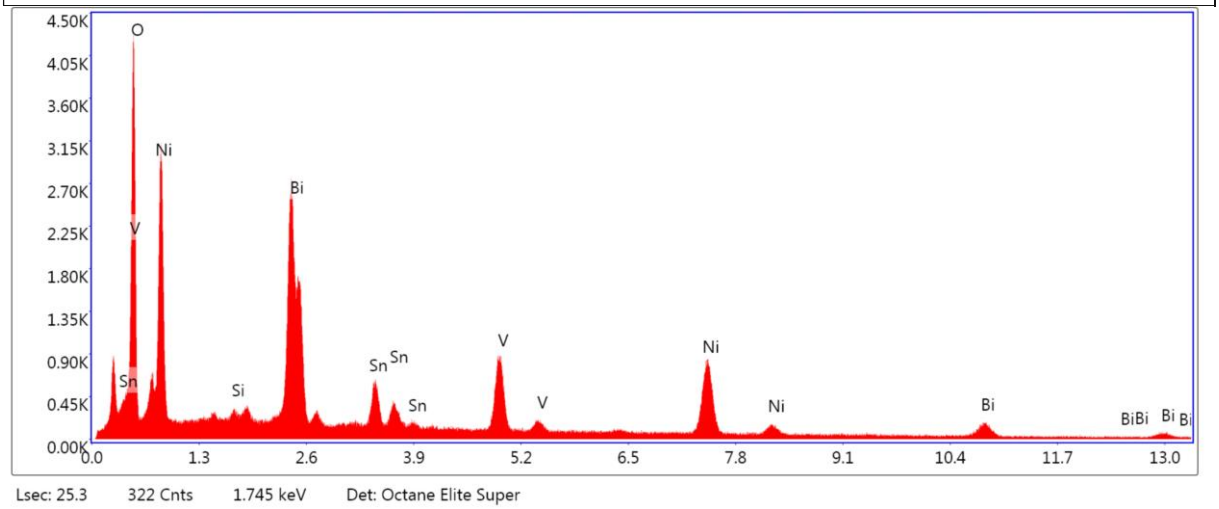

drop-cast Ni/$BiVO_4$ – FA el. – Spot 3		
Element	Weight %	Atomic %
BeK	56.8	80.2
C K	6.4	6.7
O K	11.3	9.0
SiK	0.1	0.0
BiM	9.5	0.6
SnL	1.4	0.1
V K	3.3	0.8
NiK	11.3	2.5